Single-Shot Imaging with Higher-Dimensional Encoding Using Magnetic Field Monitoring and Concomitant Field Correction

Frederik Testud,[1]* Daniel Gallichan,[2] Kelvin J. Layton,[1] Christoph Barmet,[3,4] Anna M. Welz,[1] Andrew Dewdney,[5] Chris A. Cocosco,[1] Klaas P. Pruessmann,[3] Jürgen Hennig,[1] and Maxim Zaitsev[1]

Purpose: PatLoc (Parallel Imaging Technique using Localized Gradients) accelerates imaging and introduces a resolution variation across the field-of-view. Higher-dimensional encoding employs more spatial encoding magnetic fields (SEMs) than the corresponding image dimensionality requires, e.g. by applying two quadratic and two linear spatial encoding magnetic fields to reconstruct a 2D image. Images acquired with higher-dimensional single-shot trajectories can exhibit strong artifacts and geometric distortions. In this work, the source of these artifacts is analyzed and a reliable correction strategy is derived.

Methods: A dynamic field camera was built for encoding field calibration. Concomitant fields of linear and nonlinear spatial encoding magnetic fields were analyzed. A combined basis consisting of spherical harmonics and concomitant terms was proposed and used for encoding field calibration and image reconstruction.

Results: A good agreement between the analytical solution for the concomitant fields and the magnetic field simulations of the custom-built PatLoc SEM coil was observed. Substantial image quality improvements were obtained using a dynamic field camera for encoding field calibration combined with the proposed combined basis.

Conclusion: The importance of trajectory calibration for single-shot higher-dimensional encoding is demonstrated using the combined basis including spherical harmonics and concomitant terms, which treats the concomitant fields as an integral part of the encoding. **Magn Reson Med 73:1340–1357, 2015. © 2014 Wiley Periodicals, Inc.**

Key words: nonlinear spatial encoding; quadratic fields; rapid imaging; higher-dimensional trajectories; local k-space, PatLoc; non-Fourier encoding; single-shot imaging; magnetic field monitoring; field probes; dynamic field camera; concomitant fields; Maxwell terms

INTRODUCTION

Single-shot magnetic resonance imaging allows image acquisition in less than 100ms , e.g. echo-planar imaging (EPI) (1), spiral (2), or other types of trajectories (3–5). Such short acquisition times are achieved by switching the linear spatial encoding magnetic fields (SEMs), commonly referred to as gradients, with large maximal amplitudes as fast as possible over an extended total readout time. The actual trajectory can deviate significantly from the desired trajectory (6). These deviations originate from many sources including field drifts, eddy currents, hardware delays, and concomitant fields. Without adequate correction, these inaccuracies can cause blurring, geometric distortions, or ghosting in the reconstructed images (7). The problems have been partially addressed by characterizing the eddy currents (8), by measuring the k-space trajectory, (6) and by correcting for distortions due to concomitant fields (9).

Magnetic field monitoring has been extended to imaging applications by acquiring the signal of miniature integrated sample-probe assemblies (10–17) during the imaging experiment. The field probes' signal phase is used to model the field evolution. High-quality images from spiral (11,12) or echo-planar (12) trajectories in the presence of undesirable field perturbations have successfully been reconstructed using the trajectory measured with four probes. The actual fields are only approximating the SEMs nominal spatial distribution and therefore must be described by a low order spherical harmonic expansion. Additionally, the magnetic fields produced by eddy currents are also generated by conductive structures other than the SEM coils, and therefore have higher order spherical harmonics. The higher order field changes can be monitored by using more field probes than the number of SEMs used for imaging. Barmet et al. (14) proposed a dynamic field camera with 16 field probes which allowed to measure higher order magnetic field evolutions described by real-valued spherical harmonics up to third order, which was used in the image reconstruction for echo-planar diffusion imaging (16).

Recently, the concept of using nonlinear nonbijective SEMs for imaging together with conventional linear

[1]Department of Radiology, Medical Physics, University Medical Center Freiburg, Freiburg, Germany.

[2]Centre d'Imagerie BioMédicale, Ecole Polytéchnique Fédérale de Lausanne, Lausanne, Switzerland.

[3]Institute for Biomedical Engineering, University of Zürich and ETH Zürich, Zürich, Switzerland.

[4]Skope Magnetic Resonance Technologies, Zürich, Switzerland.

[5]Siemens AG, Healthcare Sector, Erlangen, Germany.

Grant sponsor: German Federal Ministry of Education and Research (INUMAC Project); Grant number: #01EQ0605 and #13N9208; Grant sponsor: European Research Council Advanced Grant "OVOC"; Grant number: #232908; Grant sponsor: European Research Council Starting Grant "RANGEmri"; Grant number: #282345.

*Correspondence to: Federik Testud, Department of Radiology, Medical Physics, University Medical Center Freiburg, Breisacher Str. 60a, D-79106 Freiburg, Germany. E-mail: frederik.testud@uniklinik-freiburg.de

Received 16 September 2013; revised 12 February 2014; accepted 11 March 2014

DOI 10.1002/mrm.25235

Published online 31 March 2014 in Wiley Online Library (wileyonlinelibrary.com).

SEMs has been introduced as PatLoc (Parallel Imaging technique using Localized gradients) (18–20), and the closely related concept of O-Space imaging (21,22). The PatLoc reconstructed images show a lower resolution at the center of the Field-of-View (FoV) and an increasing resolution toward the edge of the FoV (23).

The resolution loss in the center of the FoV can be overcome by simultaneous use of linear and nonlinear SEMs, referred to here as higher-dimensional encoding. Gallichan et al. proposed a multishot 4D Radial-In-Out (4D-RIO) trajectory (24) allowing the preservation of the spatially varying encoding resolution while avoiding the total resolution loss in the center of the FoV. O-Space (21), Null-Space (25), and multidimensionally encoded magnetic resonance imaging (26) are other examples of recent higher-dimensional encoding methods.

Higher-dimensional encoding trajectories can also be performed in a single-shot as presented by Layton et al. (27) where the trajectory referred to as North-West Echo-Planar Imaging (NW-EPI) was designed such that a region of interest has a higher resolution than the rest of the image. A single-shot version of the 4D-RIO trajectory was recently presented in abstract form in (28). However, images reconstructed using the nominal 4D-RIO and NW-EPI trajectory showed signal voids and geometric distortions. Preliminary analysis of the trajectory deviations indicated that concomitant fields associated with strong SEMs play an important role in the observed phenomena.

Typically, imaging at higher field strengths is performed without considering the full magnetic field vector $\vec{B}(\vec{r},t)$ of the SEMs but only its z-component $B_z(\vec{r},t)$. The concomitant field (29) (often referred to as Maxwell terms) can be calculated analytically and taken into account in the image reconstruction (7) as an additional phase term which is dependent on the squared SEM waveform and on the field strength. An important property of the concomitant phase is that it cannot be refocused by switching the SEM waveform polarity and therefore accumulates during long readouts.

The concomitant fields of the linear SEMs are negligible for most imaging sequences on the clinical scanners, but can be observed in sequences particularly sensitive to them such as diffusion (30) and steady state free precession (31), and can be particularly problematic for SEM coils with an asymmetric winding pattern (32).

In this work, a dynamic field camera with 16 proton field probes was used to calibrate for the spatiotemporal field evolution (14,16,17). The two previously proposed single-shot higher-dimensional trajectories, 4D-RIO and NW-EPI, were calibrated to demonstrate the importance to take the concomitant field spatial distribution into account. In the Theory section, the concomitant field is calculated analytically up to the full second order real-valued spherical harmonic expansion and for the prototype custom-built head-insert coil (20) producing SEMs of the type S2 ($2xy$) and C2 (x^2-y^2). A novel basis for trajectory calculation from the field probes' phase is set up incorporating the spatial dependencies of the linear and the quadratic SEMs and the most important components of the concomitant field. The spatial dependencies are used to fit the acquired signal phase from the dynamic field camera to obtain the trajectory that is used for image reconstruction. Phantom and in vivo experiments were performed and were reconstructed using the nominal trajectory, the measured trajectory using real-valued spherical harmonics as basis functions and the measured trajectory using a basis combining real-valued spherical harmonics and analytically derived concomitant fields terms.

THEORY

Concomitant Fields of Quadratic SEMs

Single-shot higher-dimensional trajectories are very demanding on both linear and quadratic SEM coils, and involve an extended readout with multiple gradient echoes. They are expected to be particularly sensitive to the concomitant field terms as these are proportional to the integral of the square of the SEM amplitude. The concomitant fields $B_c(\vec{r},t)$ are defined as the difference between the length of the magnetic field vector $||\vec{B}(\vec{r},t)||$ and the sum of the main static field B_0 and all $\mathrm{SEM}_i(\vec{r})$ with amplitude $G_i(t)$. Thus $B_c(\vec{r},t)$ is equal to

$$\begin{aligned} B_c(\vec{r},t) &= ||\vec{B}(\vec{r},t)|| - B_z(\vec{r},t) \\ &= ||\vec{B}(\vec{r},t)|| - B_0 - \sum_i G_i(t)\mathrm{SEM}_i(\vec{r}). \end{aligned} \quad [1]$$

The concomitant field for arbitrary SEMs can be derived based on Gauss's law for magnetism $\vec{\nabla}\cdot\vec{B}(\vec{r},t) = 0$ and Amperè's law $\vec{\nabla}\times\vec{B}(\vec{r},t) = 0$ because currents within the imaging volume are typically zero or negligible. Ampère's law leads to

$$\frac{\partial B_x}{\partial y} = \frac{\partial B_y}{\partial x} = g, \frac{\partial B_y}{\partial z} = \frac{\partial B_z}{\partial y}, \frac{\partial B_x}{\partial z} = \frac{\partial B_z}{\partial x}, \quad [2]$$

where the explicit time and spatial dependencies have been omitted to keep the notation simpler. The parameter g can be chosen arbitrarily, it can thus be a function of space and time. In standard systems, however, g can be set to 0 (29).

The divergence equation of the Maxwell magnetostatics equations $\vec{\nabla}\cdot\vec{B} = 0$ requires additionally

$$\frac{\partial B_x}{\partial x} + \frac{\partial B_y}{\partial y} + \frac{\partial B_z}{\partial z} = 0. \quad [3]$$

$\partial B_z/\partial z$ can be explicitly calculated from the applied SEMs. Then a dependency between $\partial B_x/\partial x$ and $\partial B_y/\partial y$ is gained by introducing the dimensionless parameter α, describing the relative strength of the concomitant fields produced by the SEMs along the x- and the y-axes (32). Equation [3] can then be rewritten as

$$\frac{\partial B_x}{\partial x} = -\alpha\frac{\partial B_z}{\partial z} \quad \text{and} \quad \frac{\partial B_y}{\partial y} = -(\alpha-1)\frac{\partial B_z}{\partial z}. \quad [4]$$

In standard clinical systems, the SEM coils have cylindrical forms which requires $\alpha = 0.5$ (29). Different geometries of the SEM coils will lead to different values for α as reported by (32).

The concomitant field can be determined by approximating the $\vec{B}$ field using a Taylor expansion around the

main static field B_0. The derivation is performed in scanner coordinates with B_0 in the $+\hat{z}$ direction. By neglecting the second and higher order terms, the Taylor expansion reduces to

$$\vec{B} - B_0\hat{z} = \left(\vec{r}\cdot\vec{\nabla}\right)\vec{B} \qquad [5]$$

$$\begin{pmatrix} B_x \\ B_y \\ B_z - B_0 \end{pmatrix} = \begin{pmatrix} \frac{\partial B_x}{\partial x} & \frac{\partial B_x}{\partial y} & \frac{\partial B_x}{\partial z} \\ \frac{\partial B_y}{\partial x} & \frac{\partial B_y}{\partial y} & \frac{\partial B_y}{\partial z} \\ \frac{\partial B_z}{\partial x} & \frac{\partial B_z}{\partial y} & \frac{\partial B_z}{\partial z} \end{pmatrix} \cdot \begin{pmatrix} x \\ y \\ z \end{pmatrix}. \qquad [6]$$

The derivation in (29) for the linear $\mathrm{SEM}_{x,y,z}$ can be extended to quadratic fields, e.g. all five second order $\mathrm{SEM}_{a,b,c,d,e}$ from the real-valued spherical harmonics expansion. The derivations were confirmed using the Symbolic Math Toolbox in MATLAB (The MathWorks, Natick, MA). Explicit calculations for specific cases are shown in Appendix A.

The concomitant field expression for all SEMs up to second order Eq. [A12] can be simplified for special cases. For example, the head-insert coil from (19) produces three quadratic SEMs which, including the three linear SEMs, simplifies the general concomitant field expression given by Eqs. [A12] to [A19] (33).

The concomitant field of the quadratic encoding fields of the prototype custom-built PatLoc SEM coil (20), referred in the following simply as the PatLoc SEM coil, is of interest in this article. The encoding fields C2 and S2 of the PatLoc SEM coil (20) are rotated by approximately $\pi/8$ and $-\pi/8$ around the z-axis (scanner coordinates) to reduce coupling with the second order shims and are therefore referred in the following as SEM_α and SEM_β, respectively. The rotated x, y coordinates are denoted as x_r, y_r. The encoding fields can therefore be approximated by

$$\mathrm{SEM}_\alpha = \Re\left([(x+iy)e^{-i\frac{\pi}{8}}]^2\right) = \left(x_r^2 - y_r^2\right)$$
$$= \left(\left(x\cos\left(\frac{\pi}{8}\right) - y\sin\left(\frac{\pi}{8}\right)\right)^2 - \left(x\sin\left(\frac{\pi}{8}\right) + y\cos\left(\frac{\pi}{8}\right)\right)^2\right) \qquad [7a]$$

$$\mathrm{SEM}_\beta = \Im\left([(x+iy)e^{-i\frac{\pi}{8}}]^2\right) = 2x_r y_r$$
$$= 2\left(x\cos\left(\frac{\pi}{8}\right) - y\sin\left(\frac{\pi}{8}\right)\right)\left(x\sin\left(\frac{\pi}{8}\right) + y\cos\left(\frac{\pi}{8}\right)\right). \qquad [7b]$$

Hereafter, the factor two in the analytical description of SEM_β in Eq. [7b] is omitted because only the spatial dependencies are of importance in the following analysis. In Appendix B, the derivation of $B_c(\vec{r},t)$ is presented in detail. $B_c(\vec{r},t)$ of the PatLoc SEM coil in Eq. [B8] can be sorted as follows

$$\begin{aligned} B_c(\vec{r},t) &= ||\vec{B}|| - B_z \\ &= \frac{1}{2B_0}[(x^2+y^2)g^2 + z(x^2+y^2)2\sqrt{2}g(G_\beta - G_\alpha) + \\ &+ z^2(x^2+y^2)4\left(G_\alpha^2 + G_\beta^2\right) + \\ &+ yz2\left(gG_x + 2(\alpha-1)G_zG_y\right) + \\ &- xy2gG_z + xz2\left(gG_y - \alpha G_xG_z\right) + \\ &+ z^2\left(G_x^2 + G_y^2\right) + y^2G_z^2(1-2\alpha) + (x^2+y^2)\alpha^2G_z^2 + \\ &+ z^2x2\sqrt{2}\left(G_xG_\beta - G_yG_\alpha + G_yG_\beta + G_xG_\alpha\right) + \\ &+ z^2y2\sqrt{2}\left(-G_yG_\beta - G_xG_\alpha + G_xG_\beta - G_yG_\alpha\right) + \\ &+ xyz2\sqrt{2}G_z\left(G_\alpha - G_\beta\right) + \\ &- zx^2 2\sqrt{2}\alpha G_z(G_\alpha + G_\beta) + \\ &+ zy^2 2\sqrt{2}G_z(G_\alpha + G_\beta)(1-\alpha)]. \end{aligned} \qquad [8]$$

It is important to point out that the terms $z(x^2+y^2)$ and $z^2(x^2+y^2)$ are only arising from the quadratic SEMs. Additionally, it is to be noted that the elements x^2, y^2, z^2, x^2+y^2, xz^2, yz^2, (x^2+y^2), $z(x^2+y^2)$, and $z^2(x^2+y^2)$ are not solutions of the Laplace equation and therefore cannot be described by real-valued spherical harmonics. The elements z^2 and (x^2+y^2) are already present in the concomitant field of linear SEMs on clinical scanners, see Eq. [A13] and (29). These terms are not solutions of the Laplace equation and might need to be taken into account when doing imaging experiments with certain SEM coils, e.g., (32).

Adapted Signal Equation

The effect of the concomitant field $B_c(\vec{r},t)$ introduces an additional phase term $\phi_c(\vec{r},t)$ in the signal equation which needs then to be taken into account in the image reconstruction, either by calculating the analytical representation of the concomitant field $B_c(\vec{r},t)$ (29), from magnetic field simulations of the particular SEM coil or by field measurements of the concomitant fields (20). $\phi_c(\vec{r},t)$ can be calculated from $B_c(\vec{r},t)$ as

$$\phi_c(\vec{r},t) = \gamma\int_0^t B_c(\vec{r},\tau)\mathrm{d}\tau, \qquad [9]$$

with B_c in tesla and γ the gyromagnetic ratio. The signal equation of the spin density $\rho(\vec{r})$ for the radiofrequency (RF) channel n is then given by the following equation, extended by the phase ϕ_c (Eq. [9])

$$S_n(t) \propto \int \mathrm{d}\vec{r}\,\rho(\vec{r})c_n(\vec{r})e^{-i\phi_e(\vec{r},t)}e^{-i\gamma\Delta B_0(\vec{r})t}e^{-i\phi_c(\vec{r},t)} \qquad [10]$$

where $c_n(\vec{r})$ corresponds to the sensitivity maps of the RF channel n, $\phi_e(\vec{r},t)$ the encoding phase and ΔB_0 the magnetic field inhomogeneity distribution. The encoding phase is given by

Table 1
The Basis Ξ Corresponds to the Real-Valued Expansion of the Spherical Harmonics up to Third Order and the Basis Υ Replaces Some of These (Shown in Bold) with Terms which are Not Solutions to the Laplace Equation, But which Better Describe the Spatial Variation of the Expected Concomitant Field (see Eq. [8])

Index	Basis Ξ: real-valued spherical harmonics	Basis Υ: spherical harmonics and concomitant field terms
0	Constant	Constant
1	x	x
2	y	y
3	z	z
4	xy	xy
5	zy	zy
6	$3z^2-(x^2+y^2+z^2)$	$\boldsymbol{x^2+y^2}$
7	zx	zx
8	x^2-y^2	x^2-y^2
9	$3yx^2-y^3$	$\boldsymbol{x^2z}$
10	xyz	xyz
11	$y(5z^2-(x^2+y^2+z^2))$	$\boldsymbol{y^2z}$
12	$5z^3-3z(x^2+y^2+z^2)$	$\boldsymbol{xz^2}$
13	$x(5z^2-(x^2+y^2+z^2))$	$\boldsymbol{yz^2}$
14	$z(x^2-y^2)$	$\boldsymbol{x^2z^2}$
15	x^3-3xy^2	$\boldsymbol{y^2z^2}$

$$\phi_e(\vec{r},t)=\vec{k}(t)\cdot\vec{\psi}(\vec{r})=\gamma\int_0^t\vec{G}(\tau)\cdot\vec{\psi}(\vec{r})\mathrm{d}\tau \qquad [11a]$$

$$\text{with}\quad \vec{k}(t)=\gamma\int_0^t\vec{G}(\tau)\mathrm{d}\tau, \qquad [11b]$$

$$\vec{G}(t)=\left[G_x(t)\ G_y(t)\ G_z(t)\ G_\alpha(t)\ G_\beta(t)\right], \qquad [11c]$$

and

$$\vec{\psi}(\vec{r})=\left[\mathrm{SEM}_x(\vec{r})\ \mathrm{SEM}_y(\vec{r})\ \mathrm{SEM}_z(\vec{r})\ \mathrm{SEM}_\alpha(\vec{r})\ \mathrm{SEM}_\beta(\vec{r})\right], \qquad [11d]$$

where $\vec{k}(t)$ corresponds to the multidimensional phase coefficients. If only linear SEMs are present, the phase coefficient $\vec{k}(t)$ corresponds to the conventional k-space definition.

Trajectory Estimation from Field Probes

In (12,16), the trajectory is estimated from the measured signal phase $\phi(t)$. The signal phase can be written as

$$\phi_\eta(t)=\vec{k}(t)\cdot\vec{p}_\eta+\omega_{\eta,\mathrm{ref}}\,t+\phi_\eta(t=0), \qquad [12]$$

with $\omega_{\eta,\mathrm{ref}}$ its off-resonance frequency, $\phi_\eta(t=0)$ the phase value at time point 0, and $\vec{k}(t)$ the phase coefficients as defined by Eq. [11b]. $\vec{p}_\eta$ is the basis function evaluated at the position $\vec{r}_\eta=(x_\eta,y_\eta,z_\eta)$ of field probe η. Solving Eq. [12] in the least-square sense yields

$$\vec{k}(t)=(\mathbf{P}^T\mathbf{P})^{-1}\mathbf{P}^T[\vec{\phi}(t)-\vec{\omega}_{\mathrm{ref}}\,t-\vec{\phi}_0], \qquad [13]$$

where $\vec{\omega}$ and $\vec{\phi}$ are the vector notation of the 16 field probes' off-resonance frequency and phase, respectively. The probes' off-resonance frequency and position can be determined experimentally. **P** is the probing matrix (12) which reflects the basis constructed using the field probes' position $\vec{r}_\eta$. The real-valued spherical harmonics expansion up to third order is the basis typically used, which leads **P** to

$$\mathbf{P}=\begin{pmatrix}1 & x_1 & y_1 & z_1 & x_1y_1 & \dots & x_1^3-3x_2y_2^2\\ 1 & x_2 & y_2 & z_2 & x_2y_2 & \dots & x_2^3-3x_2y_2^2\\ \vdots & \vdots & \vdots & \vdots & \vdots & \dots & \vdots\\ 1 & x_{16} & y_{16} & z_{16} & x_{16}y_{16} & \dots & x_{16}^3-3x_{16}y_{16}^2\end{pmatrix}, \qquad [14]$$

where 16 field probes are used, resulting in a matrix **P** with dimensions 16×16. The constant in the first column of **P** corresponds to the offset of B_0 and subsequently after fitting of the probe phases with Eq. [13], $k_0(t)$ describes the drift of B_0. The conditioning of **P** is important for the calculation of Eq. [13], and is directly influenced by the field probe positions $\vec{r}_\eta$. Previously described experiments, such as in (16), have used real-valued spherical harmonics up to the third order as the chosen basis. This basis is referred to as Ξ and the resulting measured trajectory as $\vec{k}_\Xi$. As pointed out in Barmet et al. (12) Eq. [13] is generally valid for any basis.

The effect of the concomitant fields can be considered by constructing a new basis Υ to take into account the spatial dependency of the concomitant field given by Eq. [8]. Both bases are listed in Table 1. $\vec{k}_\Upsilon$ is the corresponding trajectory. The new basis allows to simplify Eq. [10] by including the concomitant field phase $\phi_c(\vec{r},t)$ in the encoding phase, $\phi_e(\vec{r},t)$, by defining $\vec{\psi}$ in Eq. [13] with the SEMs defined in basis Υ.

Basis Υ is constructed to have a constant term, the three linear terms and the two quadratic encoding fields C2 and S2 created by the PatLoc SEM coil, which are the basis functions 0, 1–3 and 4 and 8 in Table 1, respectively. Additionally, the concomitant field terms in Eq. [8] with amplitude dependent on $G_\alpha(t)$ and $G_\beta(t)$ are considered the most important terms of the real-valued spherical harmonic expansion, giving seven functions to be added to basis Υ. The x^2+y^2 term is the eigth function which is included to basis Υ because it is dependent on the arbitrary function $g(t)$.

We emphasize again that these spatial dependencies are not all solutions of the Laplace equation. The z^2 and

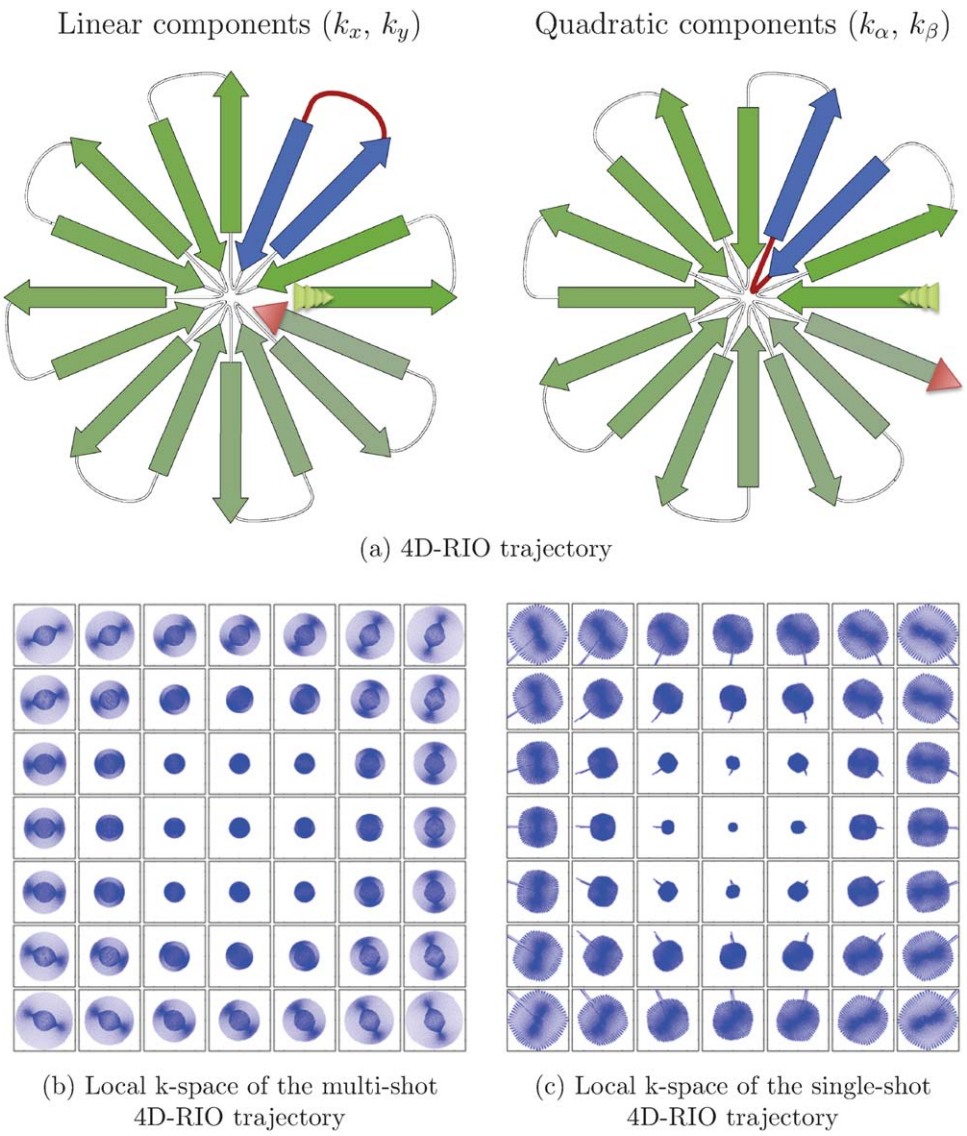

FIG. 1. **a**: Schematic representation of the linear (k_x, k_y) and quadratic (k_α, k_β) components of the single-shot 4D-RIO trajectory. The start of the trajectories is marked by multiple green triangles, and the end by the red squares. The local k-space of the multishot and the single-shot 4D-RIO are depicted in (**b**) and (**c**), respectively.

y^2 terms were not included in basis Υ as they are only dependent on linear SEM amplitudes.

The remaining three terms are chosen to be functions 5, 7, and 10 from the real-valued spherical harmonics expansion (cf. basis Ξ, Table 1), where the functions 5 and 7 are also present in the concomitant field of linear SEMs (cf. concomitant field expression for linear SEMs Eq. [A13]).

METHODS

4D-RIO Trajectory

The 4D-RIO trajectory (24) simultaneously covers both the linear (k_x, k_y) and quadratic (k_α, k_β) k-spaces with radial spokes, but with staggered timing such that the edge of (k_x, k_y)-space is reached concurrent to passing through the center of (k_α, k_β)-space, and vice-versa. The original multishot trajectory was implemented by a dual-echo sequence (24). To implement a single-shot version of 4D-RIO (28), each traversal between the center and the edge of these 2D k-spaces is treated as a separate element of the trajectory and then these elements are arranged to connect them together while minimizing the distance, in 4D Euclidean space, between their ends. The single-shot trajectory is depicted in Figure 1a. These connections need to respect the maximum amplitudes and slew rates of both the linear and the quadratic SEMs, but can be designed using methods directly analogous to existing 2D or 3D approaches (34). Assuming a nominal resolution of 64×64 with a FoV of 256×256mm, it was possible to generate a 43ms readout train which fulfills these criteria using 128 "spokes," each traversing between the center and edge of both the (k_x, k_y)-space and the (k_α, k_β)-space, but in opposite directions. The local k-spaces (a concept introduced in (24) which displays the local spatial derivatives of the net encoding phase) are similar

for the multishot and the single-shot trajectory as shown in Figure 1b and c, respectively.

Validation of the Analytical Concomitant Field Description

The magnetic field $\overrightarrow{B_s}(\vec{r})$ of the PatLoc SEM coil was simulated for a current of 80 A from a model set up in the simulation software Cobham OPERA 14 3D (Cobham, Oxfordshire, UK) and the concomitant field $B_{cs}(\vec{r})$ was calculated using Eq. [1]. $B_{cs}(\vec{r})$ was then fitted to the three terms in Eq. [B9] representing the concomitant field part arising only from the PatLoc SEMs. The three terms are proportional to x^2+y^2, $z(x^2+y^2)$, and $z^2(x^2+y^2)$. $B_{cf}(\vec{r})$ is the concomitant field calculated from the fit result. The normalized root mean square error between $B_{cf}(\vec{r})$ and $B_{cs}(\vec{r})$ was used as a metric to test the validity of the analytically derived concomitant field over a spherical volume of 20 cm diameter.

Experimental Setup

All experiments were performed on a modified 3T system (MAGNETOM Trio, a Tim System, Siemens AG, Healthcare Sector, Erlangen, Germany) fitted with transmit-array hardware (35). Two quadrupolar encoding fields were generated by a prototype custom-built SEM insert-coil as previously described by Welz et al. (20). One field was rotated by 45° with respect to the other assuring that the two encoding fields are orthogonal. The encoding fields are additionally rotated with respect to the scanner's standard S2 and C2 shim fields by $\pm\pi/8$ to minimize geometric coupling between the head SEM insert coil and the shim coils. The SEM coil for each quadrupolar field can be driven with currents up to 80A using additional high-performance multichannel gradient amplifiers. The scanner architecture was modified to control both the linear and the PatLoc SEM coil, which allows for simultaneous and independent control of up to six encoding fields. The head RF coil consisted of an outer single Transmit/Receive (T/R) RF coil, used here only for excitation, surrounding an inner eight channel receive coil array used for signal reception (Siemens AG Healthcare Sector, Erlangen, Germany).

A gradient echo based imaging sequence was used for image acquisition and control of the field probes. The sequence allowed specification of arbitrary waveforms for each of the five encoding SEM channels.

Dynamic Field Camera

A dynamic field camera consisting of an array of 16 ^{1}H field probes (14,16) was built for magnetic field estimation. Thirty 20cm long tubes with an inner and outer diameter of 2.8 and 3.2cm, respectively, were arranged in a honeycomb-like shape; inside some of these tubes the probes were placed. The field probe array was then firmly positioned inside the eight channel head RF receive coil to minimize uncontrolled mechanical vibrations during the switching of the encoding fields. The field probes were placed in four transversal planes separated by $\approx$ 3cm from each other. In each plane, four field probes were placed on a circle. On the two outer planes, the diameter of the circle was $\varnothing_1 \approx 10$cm and on the two inner planes, the diameter was $\varnothing_2 \approx 16$cm. The field probe array inside the receive coil is shown in Figure 2a. A separate Transmit (Tx) chain offered the possibility to operate the field probes in T/R mode (13) independently from the scanner and made sure that the same RF power is distributed to each probe. The Tx chain was controlled via the optical trigger from the scanner. The Tx chain consist of a signal generator (N5181A, Agilent, Santa Clara, CA), an RF power amplifier (75A400, Amplifier Research, Souderton, PA) and a 24 way Wilkinson power splitter (MITEQ-ESTONIA, Estonia). This setup is based on work presented in (13,14,16). The field probes were connected to the spectrometer of the scanner and the signal was sampled with an ADC dwell time of 2.5μs to be suitable for fast imaging. Figure 2b depicts the connection setup of the dynamic field camera to the patient table of the scanner. Solenoid baluns to minimize coupling between the RF coaxial cables were positioned between the preamplifier and the scanner plug for cables longer than 20cm. The RF coaxial cables between the field probes and the T/R switch were manually positioned until minimal coupling was observed in the acquired free induction decays. If the probes' coaxial cable positions are not carefully arranged, the coupling between the field probes can lead to phase oscillations with amplitudes up to 0.1rad and reduced signal-life time (data not shown here) which might corrupt the trajectory fit when using Eq. [13].

Trajectory Calibration

To account for possible synchronization errors between all five gradient channels, residual eddy currents and concomitant fields simultaneously, the single-shot 4D-RIO and NW-EPI trajectory were measured in a separate acquisition with the previously described dynamic field camera. The head RF coil array was kept in the SEM coil and connected to a custom-built coil test-bench for detuning and grounding during the trajectory calibration measurements. The averaged off-resonances $\vec{\omega}_{\text{ref}}$ were calculated from the phase of 10 free induction decay signals using a repetition time of TR = 1s. The position of the probes was estimated by a linear fit to the acquired phase from three projections along the spatial directions. Again 10 repetitions were acquired for averaging, with TR = 1s.

The root mean square deviation (RMSD) was estimated between the calculated and the nominal trajectory components. They are referred to as RMSD_Ξ, RMSD_Υ for the trajectories $\vec{k}_\Xi$ and $\vec{k}_\Upsilon$, respectively.

The theoretical phase evolution of the 4D-RIO trajectory was calculated using the simulated encoding magnetic fields of the PatLoc SEM coil and assuming perfect linearity of the linear SEMs with no concomitant field terms. The obtained phase evolution was then fitted to basis Υ in the volume where the spatial distribution of the SEM_α and SEM_β are described by Eq. [7], which is a $\pm$7cm long cylinder with 10cm radius (20). Both higher-dimensional encoding trajectories are using SEM_x, SEM_y, SEM_α, and SEM_β and transversal slices were acquired in the isocenter, therefore the concomitant field Eq. [8] can be simplified to

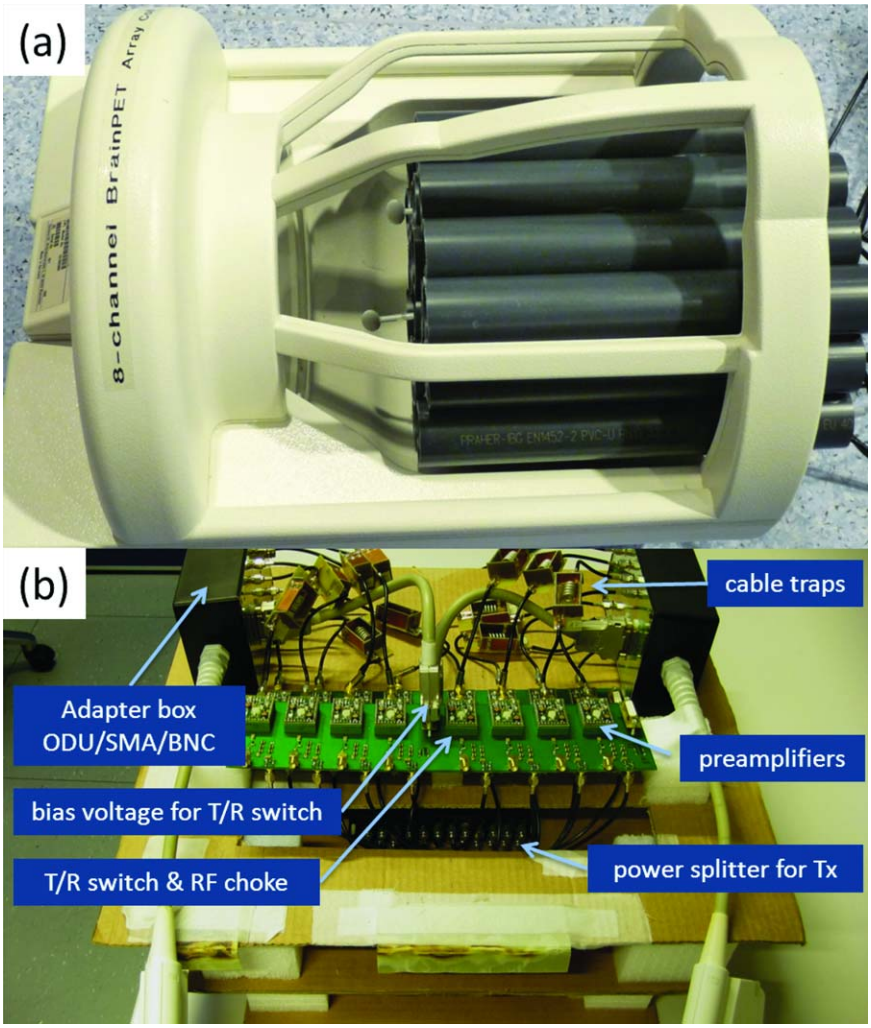

FIG. 2. **a**: Dynamic field camera setup inside the eight channel receive coil. **b**: Setup to which the 16 field probes are connected. The probes, the Wilkinson power splitter and the preamplifiers connected to the T/R switches are visible. Breakout boxes convert the scanner coil plug to SMA for the receive channels and D-sub for the PIN diodes control voltages and currents. The Wilkinson power splitter is located below the PCB board comprising the preamplifiers and the T/R switches.

$$B_c(\vec{r},t)=\frac{g^2(x^2+y^2)}{2B_0}. \qquad [15]$$

It is, therefore, expected that mainly the time-dependent coefficient $k_{Y,6}(t)$ will contribute to the image reconstruction. The RMSD was estimated between the simulated and the measured trajectory components.

Image Reconstruction

Image reconstruction was performed using an iterative conjugate gradient (CG) method including all 16 trajectory coefficients similar to the reconstruction used for non-Cartesian trajectories (36). The reconstruction was implemented in MATLAB. The coil sensitivities $c_n(\vec{r})$ and the $\Delta B_0(\vec{r})$ map of the imaged slices were acquired with a multiecho GRE sequence. The parameters were: TE $= 4, 8, 12, 16, 20, 24, 28, 32$ms, TR $= 0.1$s, flip angle 25°, a slice thickness of 5mm, and a FoV $= 220 \times 220$ mm^2 for a matrix size of 300×300. $c_n(\vec{r})$ were estimated using the adaptive method described in (37). The acquired receiver sensitivity and ΔB_0 maps were fitted to real-valued spherical harmonics as in (38) up to 20th order and recalculated on the desired reconstruction grid. $c_n(\vec{r})$ were additionally masked with a disk of diameter equal to the FoV. The disk edge was further smoothed to zero with a 2D Gaussian filter of a full width at half maximum of 19px. The CG reconstruction was implemented on a graphic processor unit (GPU) (NVIDIA Tesla C2050 GPU) allowing fast image reconstruction (39,40) as detailed in (41). The number of CG-iterations was chosen manually for each reconstruction, stopping when the best image quality was deemed to have been reached, which lead to an image reconstruction time between 19.5 and 24.8s. All images were reconstructed assuming three different effective encoding trajectories: the nominal trajectory, trajectory $\vec{k}_\Xi$, and trajectory $\vec{k}_Y$. As in (5), the data acquired during ramp up and down of the trajectory are excluded from the reconstruction to avoid crossings of the trajectory, which can cause off-resonance and T_2^* artifacts.

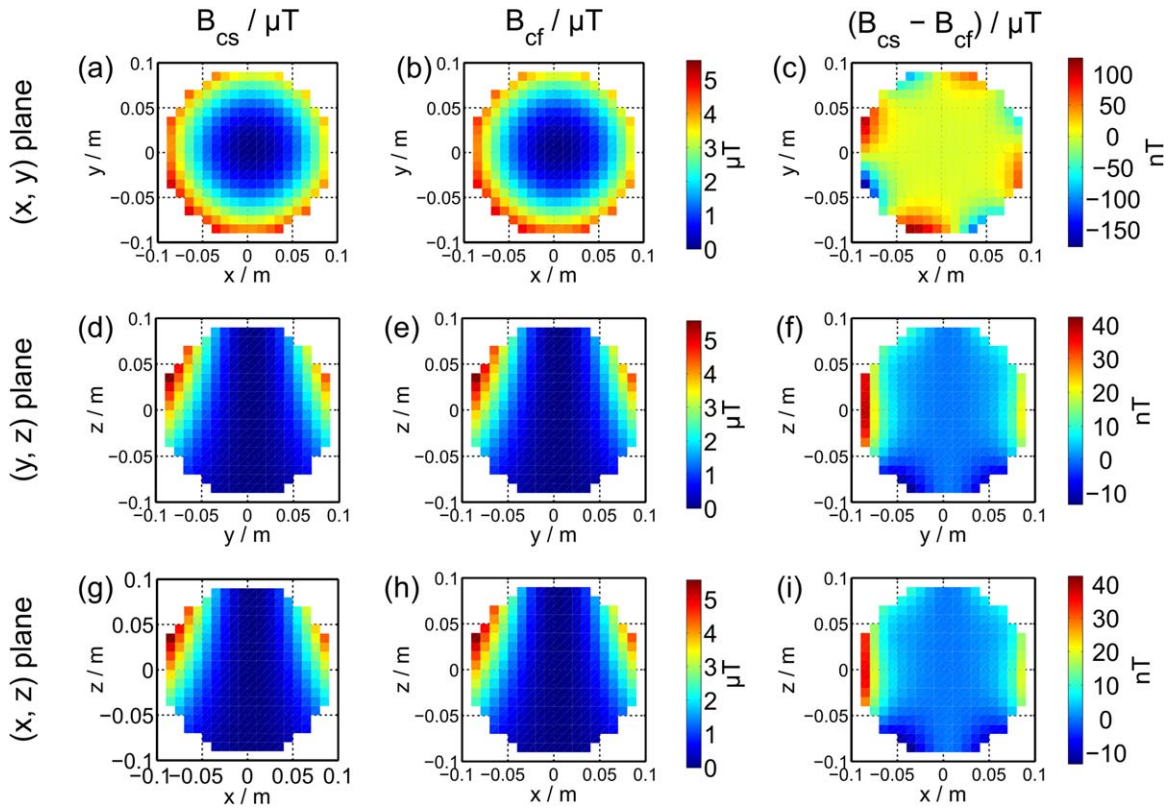

FIG. 3. The plots (**a**), (**d**), and (**g**) of the first column show the simulated concomitant fields $B_{cs}(\vec{r})$ for the $(x,\ y)$, the $(y,\ z)$, and the $(x,\ z)$ planes. The plots shown in the second column are the calculated concomitant fields $B_{cf}(\vec{r})$ from the fit result $B_{cs}(\vec{r})$ to x^2+y^2, $z(x^2+y^2)$ and $z^2(x^2+y^2)$. The plots of the first and the second column have the same colorbar. The third column shows the residual from (**b**) and (**a**). The first row shows the $(x,\ y)$ plane at $z=0\text{cm}$, the second row the $(y,\ z)$ plane at $x=0\text{cm}$ and the third row the $(x,\ y)$ plane at $y=0\text{cm}$

Phantom Experiments

The phantom consisted of a 190mm diameter plastic cylinder containing approximately 130 thin Plexiglas tubes parallel to the longitudinal axis of the cylinder. The cylinder and tubes were filled with nickel sulfate and sodium chloride doped water. The 4D-RIO acquisitions had a nominal FoV of $256\times256\text{mm}^2$ and a total readout durations of 43ms. The same acquisition dwell time of 2.5μs as for the trajectory calibration measurements was chosen. The phantom data was reconstructed on a 128 ×128 grid. Two 4D-RIO phantom experiments were performed, one without and one with eddy current correction of the nonlinear SEMs as estimated in (20). The eddy current correction is performed by the scanner as part of the pre-emphasis.

In Vivo Experiments

In vivo experiments were performed on a healthy volunteer. Informed consent was acquired prior to the experiment in accordance with the internal review board approved protocol. The same sequence parameters were used as for the phantom experiments described above. The safety for the PatLoc SEM insert was discussed in (42–44) and for higher-dimensional imaging in (44). To maintain safe operation with respect to peripheral nerve stimulation, the protocol used an incremental increase of SEM amplitudes as described in (44). The Fourier spectrum of the 4D-RIO trajectory showed dominant frequencies at 35Hz and between 1400 and 1600Hz which are outside the range of the potentially problematic resonance frequencies of the PatLoc SEM coil $480-650\text{Hz}$ (42).

NW-EPI in vivo experiments were performed, using the modified EPI trajectory as described in (27), with a FoV of 220mm and a readout time of 41.6ms. For comparison, an EPI experiment was performed as well (27). All three in vivo data sets were reconstructed on a 128 ×128 grid.

RESULTS

Validity of the Concomitant Field Description

The analytically derived concomitant field Eq. [8] originating from the PatLoc SEM coil was compared to the concomitant field calculated from magnetic field simulations of the PatLoc SEM coil. The concomitant field term from magnetic field simulation, the result of the fit and the remaining difference between simulation and fit are plotted in Figure 3. The normalized root mean square error estimated over a spherical volume of 20cm diameter is 0.1% demonstrating the good correspondence between the analytical formulas for $B_c(\vec{r})$ (Eq. [B9]) and the $B_{cs}(\vec{r})$ of the SEM coil.

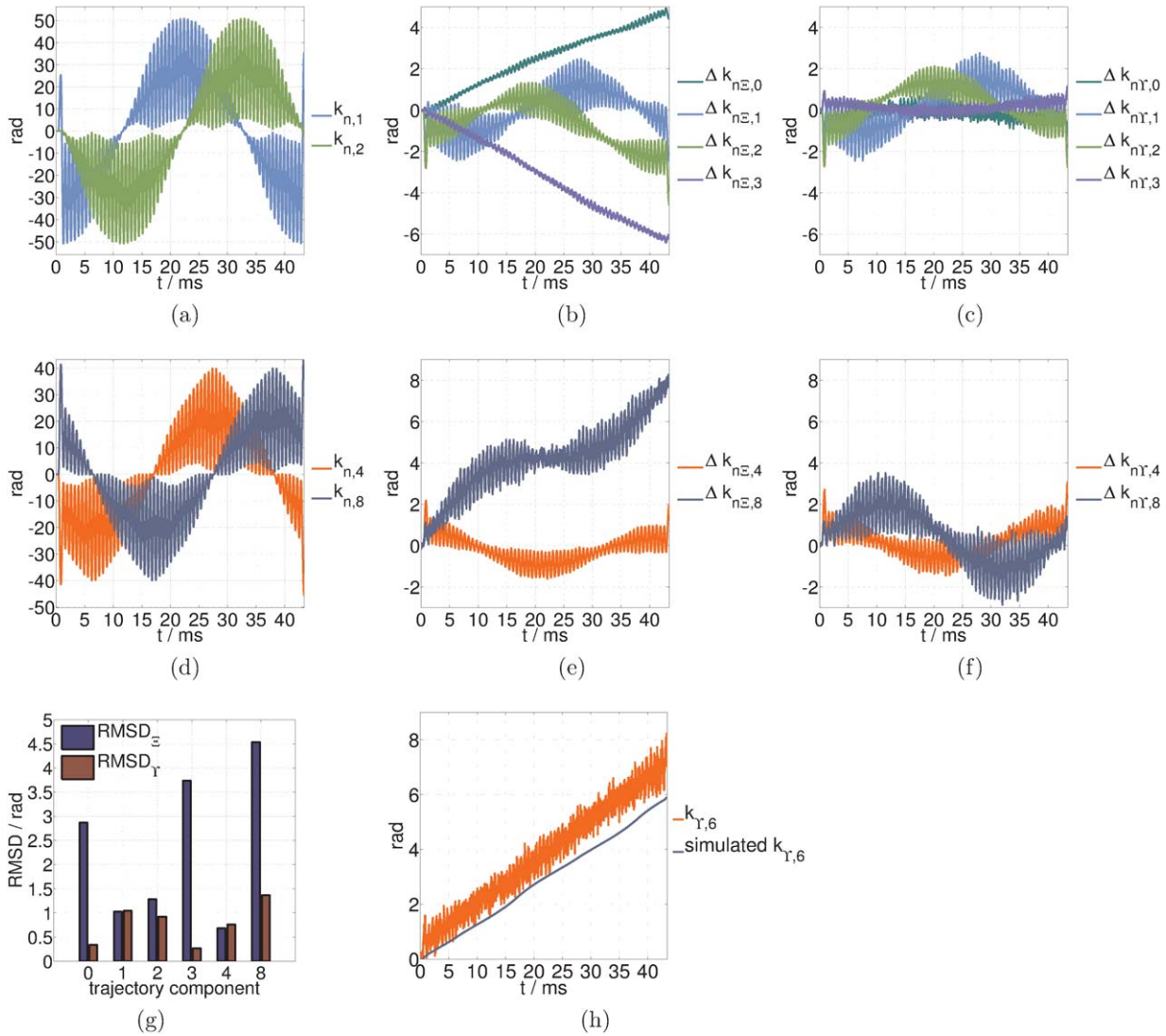

FIG. 4. **a**: Linear components of the nominal trajectory $\vec{k}_n$. **b**: difference $\Delta k_{n\Xi}$ between the zeroth and the linear components of $\vec{k}_n$ and the measured $\vec{k}_\Xi$ (basis set only using pure real-valued spherical harmonics). $k_{n,0}$ and $k_{n,3}$ are designed to be zero. **c**: Difference $\Delta k_{n\Upsilon}$ between the zeroth and the linear components of $\vec{k}_n$ and the measured $\vec{k}_\Upsilon$ (basis set including nonspherical harmonic terms to account for concomitant field terms). **d**: Quadratic components of the nominal trajectory $\vec{k}_n$. **e** and **f**: Difference between the primary quadratic components of $\vec{k}_n$ and the measured $\vec{k}_\Xi$ and $\vec{k}_\Upsilon$, respectively. The RMSD values estimated between the nominal and the measured trajectory components (0, 1, 2, 3, 4, and 8) are summarized in the bar plot shown in (**g**). In general, $\vec{k}_\Upsilon$ is closer to the nominal $\vec{k}_n$ components. **h**: Simulated and measured $k_{\Upsilon,6}$. A good agreement is observed.

4D-RIO Trajectory Fit

The linear components of the nominal trajectory $\vec{k}_n$ are shown in Figure 4a. $k_{n,4}(t)$ and $k_{n,8}(t)$ are calculated by rotating the components $k_\alpha(t)$ and $k_\beta(t)$, calculated from the waveforms $G_\alpha(t)$ and $G_\beta(t)$ of SEM_α and SEM_β as described by Eq. [7], respectively. The difference between the nominal and $\vec{k}_\Xi$ and $\vec{k}_\Upsilon$ zeroth and linear components are plotted in Figure 4b and c, respectively. The quadratic components of the nominal trajectory are depicted in Figure 4d. In Figure 4e and f, the differences between the quadratic components of the nominal and the measured trajectories are presented. The linear drift of the $k_{\Xi,0}$ and $k_{\Xi,3}$ (constant and linear SEM in z-direction) components can be reduced when using basis Υ instead of Ξ. The same is observed for the encoding components $k_{\Xi,2}$ and $k_{\Xi,8}$. This is demonstrated by the reduced RMSD values for basis Υ compared to basis Ξ which are summarized in Figure 4g. For trajectory components 1 and 4, the RMSD values are by 1.9 and 11.5% larger for k_Υ than for k_Ξ, respectively. The remaining quadratic and third order components have variations in the basis Ξ up to $\pm 6\,\mathrm{rad}$. With basis Υ variations below $\pm 3\mathrm{rad}$ in the cubic and quartic forms $k_{\Upsilon,9}$ to $k_{\Upsilon,15}$ are observed, except for $k_{\Upsilon,6}$, which is linearly increasing up to $\approx 8\mathrm{rad}$.

In general, using basis Υ, the primary linear and quadratic terms are present as well as the $k_{\Upsilon,6}$ component caused by the concomitant field derived in Eq. [8]. The condition numbers of the probing matrix $\mathbf{P}$ of basis Ξ and Υ were 57 and 106, respectively.

The simulated and the measured $k_{\Upsilon,6}$ component have a similar temporal evolution, (cf. Fig. 4h) which is reflected in a RMSD of 1rad.

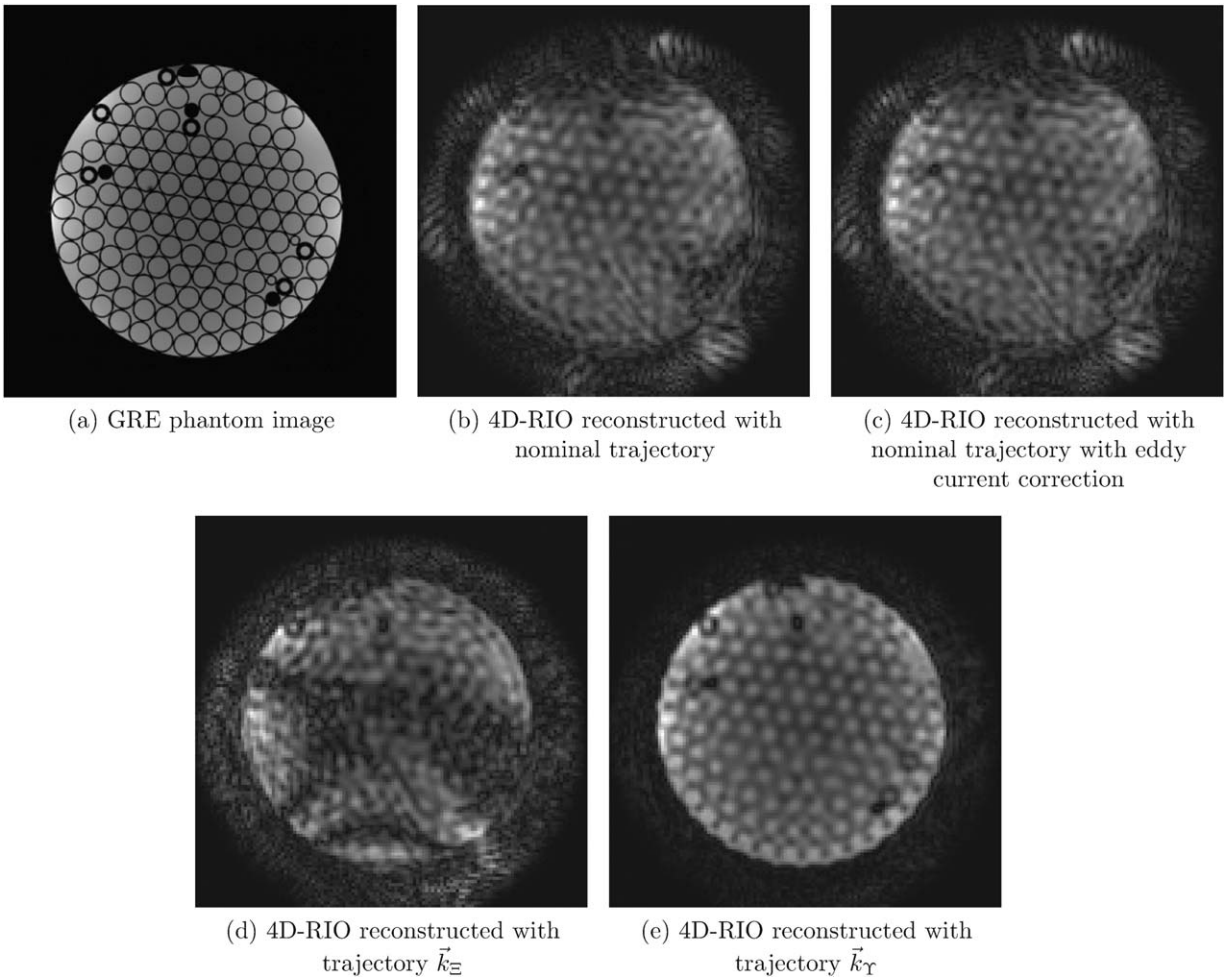

FIG. 5. **a**: Reference GRE image, enlarged from $220 \times 220\text{mm}^2$ (256×256 grid) to the same FoV of $256 \times 256\text{mm}^2$ (349×349 grid) as the 4D-RIO acquisition by adding background around the acquired image for better visual comparison. **b**: Reconstructed image using the nominal trajectory without and (**c**) with eddy current correction. **d**: Reconstructed image using the measured trajectory $\vec{k}_{\Xi}$ (basis set including only pure real-valued spherical harmonics) and (**e**) $\vec{k}_{\Upsilon}$ (basis set including nonspherical harmonic terms to account for concomitant field terms).

4D-RIO Phantom Experiment

In Figure 5, the reconstructed phantom images are shown after 20 CG-iterations. Signal voids are visible in the top and in the right part of the 4D-RIO phantom image when using the nominal trajectory, regardless of the use of eddy current correction of the nonlinear SEMs or not. Reduced artifacts outside the phantom but increased signal voids in the object are visible when performing the image reconstruction with $\vec{k}_{\Xi}$. Using $\vec{k}_{\Upsilon}$ no signal voids are visible. Comparison of Figure 5d and e clearly demonstrates the importance of taking concomitant fields into account.

4D-RIO In vivo Experiment

In Figure 6, the reconstructed in vivo images of one experiment are shown after 15 CG-iterations. Ringing and stripe artifacts are visible inside the brain when using the nominal trajectory without applied eddy current correction. Large signal voids are visible in the brain when using $\vec{k}_{\Xi}$ for the image reconstruction. The image reconstructed with the trajectory $\vec{k}_{\Upsilon}$ shows an almost artifact free image. The signal void and blurring at the frontal part of the brain is most likely due to field inhomogeneities and is—to a minor extent—also visible in the gradient echo image.

NW-EPI In vivo Experiment

In Figure 7, the reconstructed in vivo EPI and NW-EPI after 20 CG-iterations are shown. Here, only the EPI reconstructed with $\vec{k}_{\Upsilon}$ is shown as it has the smallest amount of artifacts and geometric distortions compared to EPI's reconstructed using $\vec{k}_{n}$ and $\vec{k}_{\Xi}$ (data not shown here).

As presented in (27), the NW-EPI show an increased resolution in the top left part and a reduced resolution in the bottom right part of the FoV compared to standard EPI. Strong distortions are visible in the reconstructed NW-EPI when using the nominal trajectory; they can be reduced using $\vec{k}_{\Xi}$. The geometric distortion in the posterior brain can be well corrected for when using $\vec{k}_{\Upsilon}$.

DISCUSSION

In this article, reconstructed single-shot higher-dimensional images from 4D-RIO and NW-EPI are presented which use simultaneous linear and quadrupolar fields. A

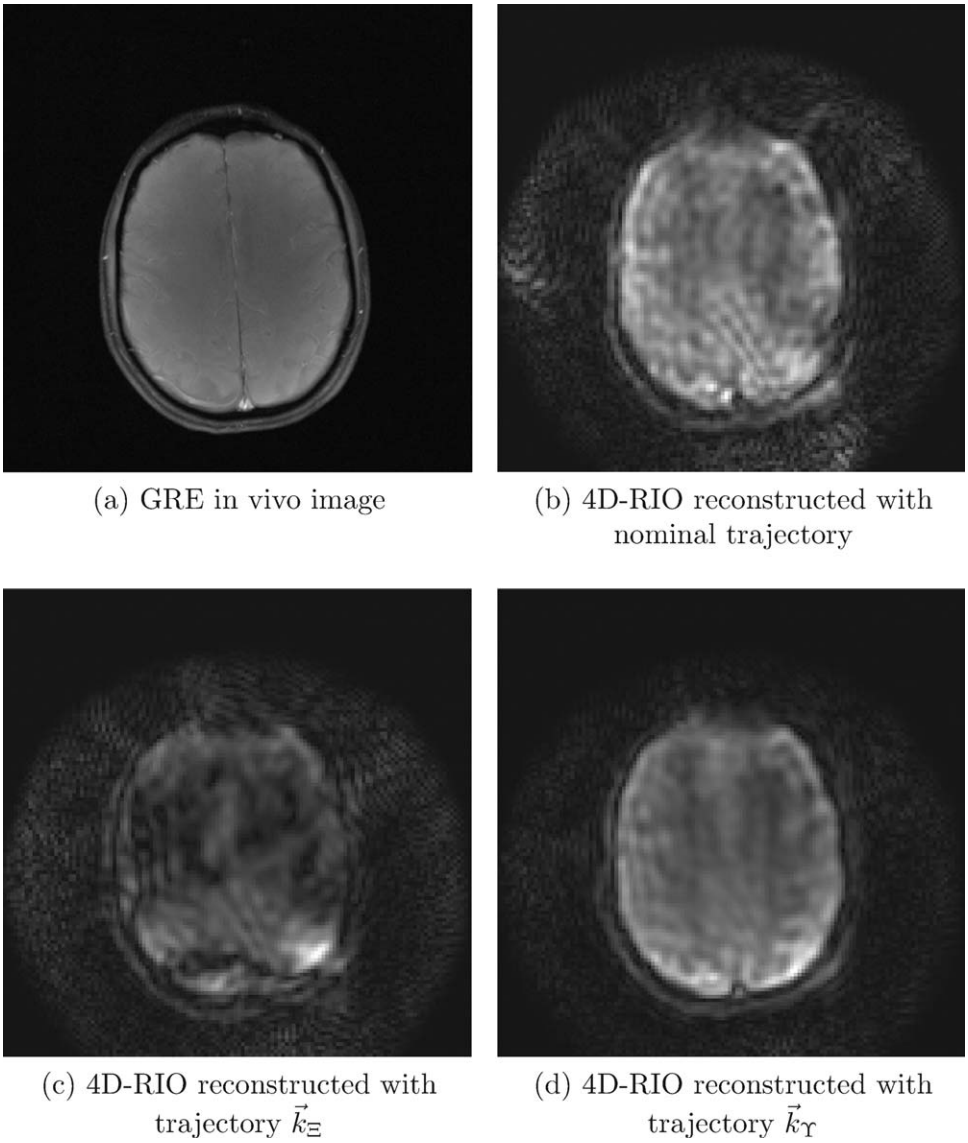

FIG. 6. **a**: Reference in vivo GRE image, enlarged from 220×220 mm^2 (256×256 grid) to the same FoV of $256 \times 256 mm^2$ (349×349 grid) as the 4D-RIO by adding background around the acquired image for better visual comparison. **b**: Reconstructed image using the nominal trajectory, (**c**) using the estimated trajectory $\vec{k}_{\Xi}$ (basis set only using pure real-valued spherical harmonics) and (**d**) using $\vec{k}_{\Upsilon}$ (basis set including nonspherical harmonic terms to account for concomitant field terms).

dynamic field camera with 16 proton-based field probes was built to calibrate the trajectory for successful image reconstruction. The proposed method is, however, not limited to the two trajectories used here, but is valid for any higher-dimensional trajectory with a long readout and large SEM amplitudes.

We derived the analytical form for the concomitant fields resulting from pure real-valued spherical harmonics, as well as for the specific design of the custom-built and the high-performance PatLoc SEM coils. In the derivation presented here, the quadrupolar fields are assumed to be rotated by 22.5° around the z-axis as in the simulations used. In the prototype custom-built coil, however, the quadropular fields are rotated by -21° and 24° for SEM_α and SEM_β, respectively (20). These small deviations are expected to only impair the coefficients in front of the spatial terms, which are irrelevant because only the spatial dependencies are of importance in this work. Terms are present in the derived formulas for $B_c(\vec{r}, t)$ in Eqs. [A12], [A19], and [8] which can not be described by spherical harmonics. For example, $(x^2 + y^2)$, $z(x^2 + y^2)$, and $z^2(x^2 + y^2)$ are not a solution of the Laplace equation. These terms are appearing because of the use of quadratic SEMs. The analytically derived formula for $B_c(\vec{r}, t)$ for the PatLoc SEM coil was compared to magnetic field simulations. The calculated root mean square error of 0.1% supports the validity of the analytical derivation. It is important to point out that the coefficient g^2 of the spatial term $x^2 + y^2$ is not zero for the PatLoc coil and justifies its presence in basis Υ, as demonstrated by the fit of the simulated phase evolution of the 4D-RIO trajectory to basis Υ. The remaining difference at the edges of the FoV (Fig. 3) is most likely due to more complex fields generated near the current paths of the PatLoc SEM coil (20), which cannot adequately be described by the assumption of purely quadratic SEMs, Eq. [7]. The comparison of the simulated with the measured trajectory $\vec{k}_{\Upsilon}$ showed a good agreement demonstrating that concomitant fields are truly measured with the field camera and corrected for in the image reconstruction. The observed mismatches can be explained by differences between the simulated quadratic fields and

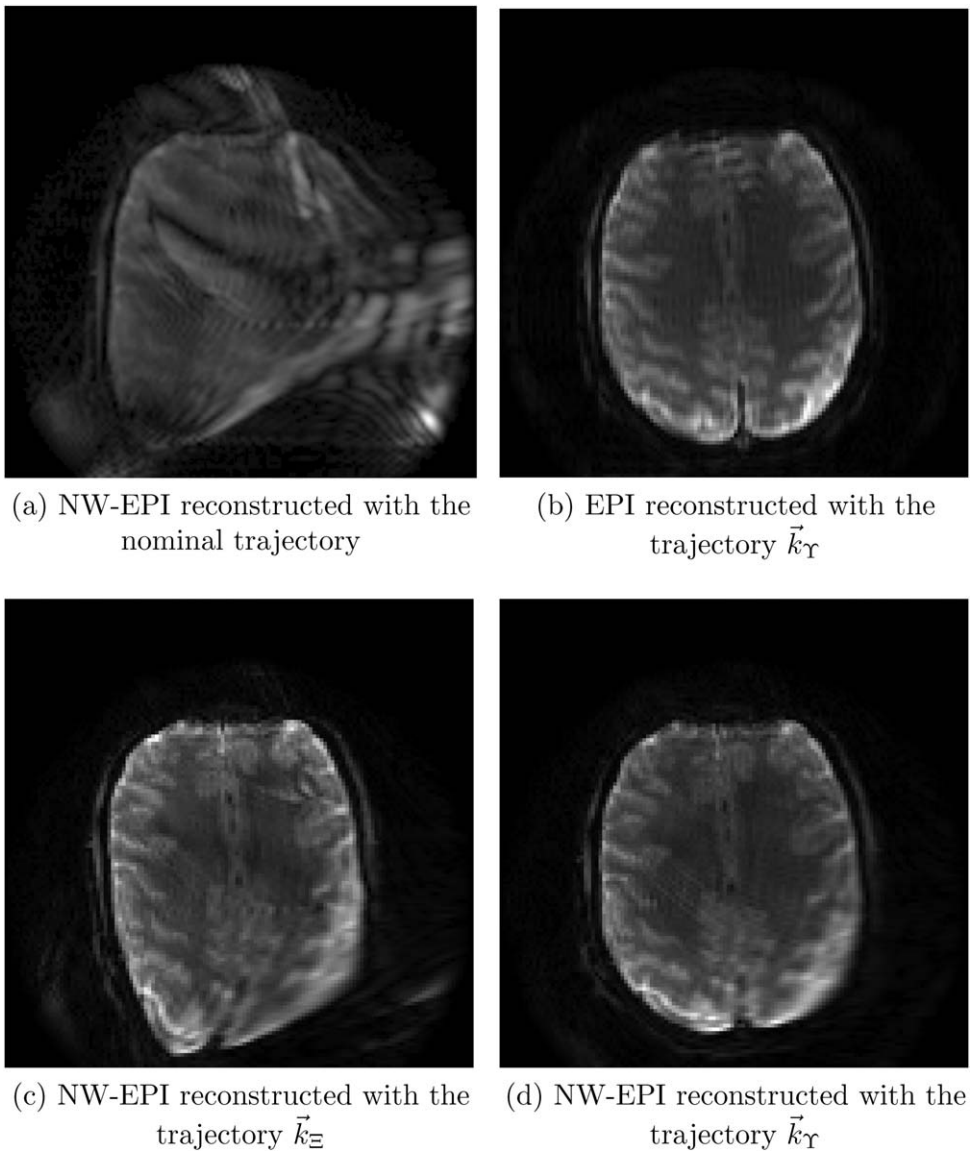

FIG. 7. **a**: NW-EPI reconstructed using the nominal trajectory and (**b**) EPI reconstructed using $\vec{k}_{\Upsilon}$ (basis set including nonspherical harmonic terms to account for concomitant field terms). **c:** NW-EPI reconstructed using $\vec{k}_{\Xi}$ (basis set only using pure real-valued spherical harmonics) and (c) using $\vec{k}_{\Upsilon}$.

the actual encoding fields of the home-built PatLoc coil (20), and also the assumption of perfectly linear SEMs with negligible concomitant components. Also, waveform corrections such as the pre-emphasis were not taken into account in the simulation of the phase evolution.

An alternative approach to the derivation of the concomitant field can be obtained from the B_x and B_y components of the SEMs by spatial differentiation of the magnetic field scalar potential obtained by solving the Laplace equation. The spatial distribution and strength of the magnetic encoding field radial component $B_r = \sqrt{B_x^2 + B_y^2}$ for linear, quadratic, and cubic SEMs were investigated in (45). The concomitant field B_c can then be calculated from

$$B_c(\vec{r}, t) = \frac{B_r^2(\vec{r}, t)}{2B_0}. \quad [16]$$

No hardware implementation details were taken into account. From the analysis performed in (45), the larger B_r of quadratic SEMs leads to concomitant terms approximately four times larger compared to the concomitant field for linear SEMs. Therefore, the effect of the concomitant fields for imaging using nonlinear SEMs is expected to have a larger impact than using linear SEMs.

The spatial dependencies present in the concomitant field formula for the combined linear and PatLoc SEMs Eq. [8] were used to create the basis Υ to fit the phase of the field probes to better describe the measured phase evolution.

The positioning of the field probes was a compromise, as it is desirable to be far from the isocenter to induce larger phase variation and improved SNR, while being too far from the isocenter may push the frequency offset outside the bandwidth of the acquired probe data. The field probes' position could be further optimized by minimizing an appropriate cost function to improve the conditioning of the probing matrix as proposed by (46). This would decrease the very large condition number of **P** for basis Υ obtained in this probes' configuration and improve the trajectory fit using Eq. [13]. Additionally, the phase of the field probes positioned near the isocenter could be filtered using, e.g. a Savitzky Golay filter

(47). However, despite the condition number for **P** for basis Υ being twice as large as the condition number for basis Ξ, a significant image quality improvement was obtained using $\vec{k}_{\Upsilon}$ for image reconstruction.

Instead of using a dynamic field camera, voxel-based phase mapping can be performed to obtain the true phase evolution for every pixel, as proposed by Schneider et al. (48). This method was used successfully for image reconstruction in O-space imaging (22). The method is very accurate but very time consuming and might not be usable for trajectory calibration in vivo. Realistically, the trajectory calibration needs to be performed via a separate experiment on a phantom. However, mechanical vibrations might change when different mechanical loads are placed in the SEM coil. The same problem is present with the current dynamic field camera setup used here. However, it can be overcome by using, e.g. fluorine (16,46) or deuterium (49) based field probes allowing concurrent field monitoring. As demonstrated in the experiments shown here, it is necessary to monitor the complete phase evolution induced by the encoding trajectory allowing to record the accumulated phase due to the concomitant field. This can only be measured with field probes which have long enough relaxation times, as was the case here. Additionally, the necessity of non-Laplacian spatial terms is demonstrated by the reconstructed images. The choice of the functions used in basis Υ was made in order to obtain good image quality. A more thorough method would be to have a dynamic field camera with more than 16 channels to extend the real-valued spherical harmonics expansion basis to all spatial terms of the concomitant field given by Eq. [8] to improve the trajectory fit result.

The differences between the nominal and the measured trajectories $\vec{k}_{\Xi}$ and $\vec{k}_{\Upsilon}$ are shown for some of the k-space components which are common to the two bases in Figure 4. The linear decrease of $k_{\Xi,3}$ when no SEM_z was applied led to the conclusion that the basis set using only solutions to the Laplace equation is not adequate. By using basis Υ, which includes terms that are not solutions to the Laplace equation, but instead follow the form expected by some of the dominant concomitant field terms, the observed drift of the components $k_{\Xi,0}$ and $k_{\Xi,3}$ can be reduced as shown by $\Delta k_{n\Upsilon,0}$ and $\Delta k_{n\Upsilon,3}$. Moreover, the primary imaging components $k_{\Upsilon,2}$ and $k_{\Upsilon,8}$ are much closer to the designed trajectory components $k_{n,2}$ and $k_{n,8}$ than when using basis Ξ. $k_{\Upsilon,6}(t)$ describes the temporal evolution of the quantity g^2 which was introduced in the derivation of $B_c(\vec{r},t)$ due to Amperè's law, Eq. [2]. For the 4D-RIO and the NW-EPI trajectories, a linear increase during the readout was observed up to 7rad and 20rad, respectively. This demonstrates the importance of the quantity g^2 for the particular SEM coil used in the experiments. All $\vec{k}_{\Upsilon}$ terms with a *z*-dependency show very small variation during the readout, as expected from the designed 4D-RIO trajectory. The same was observed for the NW-EPI trajectory.

GPU acceleration was also used for other magnetic resonance imaging reconstruction applications (39,40). The here used implementation provided fast enough processing for practical use, and it can be further accelerated by using multiple graphic processor units simultaneously (41).

For the 4D-RIO trajectory, the multiple crossing of the local k-space centers shown in Figure 1b leads to the acquisition of signals of different contrasts and consequently to a mixing of multiple contrasts. This effect might also be exploited by filtering the data to select the desired contrast, as performed for Turbo Spin Echo O-space imaging (50).

Some stripe artifacts are present in the NW-EPI and 4D-RIO in vivo images that were not observed in the phantom data. One possible explanation could be the different mechanical loading of the SEM head coil when a volunteers' head, a phantom, or a dynamic field camera is present leading to slightly different mechanical vibrations.

CONCLUSIONS

We demonstrated the importance of taking the concomitant field into account for successful image reconstruction for arbitrary single-shot higher-dimensional encoding. The trajectory was calibrated using a dynamic field camera with 16 field probes. A fitting basis was constructed for encoding field calibration that combines real-valued spherical harmonics with analytically derived concomitant field terms. In this way, the most important concomitant field terms are treated as an integral part of the encoding.

ACKNOWLEDGMENTS

The authors thank Dr. B. Zahneisen for his help with the pulse sequence programming and Marion Semmler's work in setting up the model of the PatLoc SEM coil and the Biot Savart calculations. Also, they thank Dr. E. Fischer and X. Cao for helpful discussions regarding the implementation of the dynamic field camera.

APPENDIX A

A Concomitant Fields of Quadratic Fields

In the following, a complete derivation of the concomitant field $B_c(\vec{r},t)$ produced by all second order SEMs of the real-valued spherical harmonics expansion (Table 1). The partial derivatives of B_z with the SEMs described by the linear and second order real-valued spherical harmonics defined in Cartesian coordinates as

$$\mathrm{SEM}_x(\vec{r}) = x \quad [A1a]$$
$$\mathrm{SEM}_y(\vec{r}) = y \quad [A1b]$$
$$\mathrm{SEM}_z(\vec{r}) = z \quad [A1c]$$
$$\mathrm{SEM}_a(\vec{r}) = \left(x^2 - y^2\right) \quad [A1d]$$
$$\mathrm{SEM}_b(\vec{r}) = xy \quad [A1e]$$
$$\mathrm{SEM}_c(\vec{r}) = \left(2z^2 - (x^2 + y^2)\right) \quad [A1f]$$
$$\mathrm{SEM}_d(\vec{r}) = zx \quad [A1g]$$
$$\mathrm{SEM}_e(\vec{r}) = zy \quad [A1h]$$

with their respective SEM waveforms $G_a(t), \ldots, G_e(t)$ are then

$$\frac{\partial B_z}{\partial x} = G_x + 2xG_a + yG_b - 2xG_c + zG_d \quad [A2]$$
$$\frac{\partial B_z}{\partial y} = G_y - 2yG_a + xG_b - 2yG_c + zG_e \quad [A3]$$
$$\frac{\partial B_z}{\partial z} = G_z + 4zG_c + xG_d + yG_e. \quad [A4]$$

The divergence equation of Maxwell's magnetostatics equations, Eq. [3], introduces the additional requirement

$$\frac{\partial B_x}{\partial x}+\frac{\partial B_y}{\partial y}+G_z+4zG_c+xG_d+yG_e=0. \qquad \text{[A5]}$$

By introducing the dimensionless parameter α in Eq. [A5] two more constraints are introduced

$$\begin{aligned}\frac{\partial B_x}{\partial x}&=-\alpha(G_z+4zG_c+xG_d+yG_e)\\ \text{and}\quad \frac{\partial B_y}{\partial y}&=-(G_z+4zG_c+xG_d+yG_e)(\alpha-1)\end{aligned} \qquad \text{[A6]}$$

where α describes the relative strength of the concomitant fields produced by an applied SEM_z along the x- and y-axes (32). On standard clinical systems, the linear SEMs are cylindrically symmetric requiring $\alpha=0.5$ (29) (in the case of the asymmetric coil used in (32), α is 0.22). The partial derivatives and the constraints from Maxwell's equations, Eqs. [A5] and [2], allow calculation of the magnetic field vector length $||\vec{B}||$

$$\begin{aligned}||\vec{B}(\vec{r})|| &= \sqrt{B_x^2+B_y^2+B_z^2}\\ &= \sqrt{B_x^2+B_y^2+(B_0+\sum_{i=x,y,z,a,b,c,d,e}[\mathrm{SEM}_i\times G_i])^2}\\ &= \sqrt{B_0^2(1+u)}\end{aligned} \qquad \text{[A7]}$$

$$\text{with}\quad u=\frac{B_x^2+B_y^2}{B_0^2}+2\frac{\sum_{i=x,y,z,a,b,c,d,e}[\mathrm{SEM}_i\times G_i]}{B_0}+\frac{(\sum_{i=x,y,z,a,b,c,d,e}[\mathrm{SEM}_i\times G_i])^2}{B_0^2}. \qquad \text{[A8]}$$

The Taylor expansion of $\sqrt{1+u}$ is

$$\sqrt{1+u}=1+\frac{u}{2}-\frac{u^2}{8}+\frac{u^3}{16}-\cdots \qquad \text{[A9]}$$

and using Eq. [A9] in Eq. [A8], we can reach the approximation (neglecting higher order terms)

$$\begin{aligned}||\vec{B}(\vec{r})|| &= B_0\sqrt{(1+u)}\\ &= B_0+\sum_{i=x,y,z,a,b,c,d,e}[\mathrm{SEM}_i\times G_i]+\frac{B_x^2+B_y^2}{2B_0}\\ &\quad+\mathcal{O}\big([\mathrm{SEM}_i\times G_i])^2\big)+\mathcal{O}\big(([\mathrm{SEM}_i\times G_i])^3\big)\\ &\quad+\mathcal{O}\big(([\mathrm{SEM}_i\times G_i])^4\big)++\mathcal{O}\left(\frac{1}{B_0^2}\right)+\mathcal{O}\left(\frac{1}{B_0^3}\right)\end{aligned} \qquad \text{[A10]}$$

$$\approx B_0+\sum_{i=x,y,z,a,b,c,d,e}[\mathrm{SEM}_i\times G_i]+\frac{B_x^2+B_y^2}{2B_0}. \qquad \text{[A11]}$$

Using Eqs. [1] and [A11], the concomitant field B_c for all second order real-valued spherical harmonics is then, with unknown g and α,

$$\begin{aligned}B_c=\frac{1}{2B_0}[&(G_e^2+G_d^2)z^4+((8G_cG_e\alpha+(-4G_a-12G_c)G_e+2G_bG_d)y+\\
&+(-8G_dG_c\alpha+2G_eG_b+4G_d(-G_c+G_a))x+2G_dG_x+2G_eG_y)z^3+\\
&+((16G_c^2\alpha^2+(2G_e^2-16G_c(3G_c+G_a))\alpha+4G_a^2+24G_aG_c+G_b^2+36G_c^2-2G_e^2)y^2+\\
&+((-16G_cG_b-2G_dG_e)x+(8G_yG_c+2G_eG_z)\alpha+\\
&-12G_yG_c-4G_aG_y+2G_bG_x-2G_eG_z+2G_dg)y+\\
&+(16G_c^2\alpha^2+(-2G_d^2-16G_c(-G_c+G_a))\alpha+4G_c^2+4G_a^2-8G_aG_c+G_b^2)x^2+\\
&+((-8G_cG_x-2G_dG_z)\alpha+2G_bG_y+4G_aG_x+2gG_e-4G_cG_x)x+G_y^2+G_x^2)z^2+\\
&+((-8+8\alpha)G_e(G_c\alpha-3/2G_c-1/2G_a)y^3+\\
&+((8G_c\alpha^2G_d-4G_d(G_a+5G_c)\alpha-2G_eG_b+4G_d(3G_c+G_a))x+8G_z\alpha^2G_c+\\
&+(2G_eG_y-4G_z(G_a+5G_c))\alpha+4G_aG_z+2gG_b+12G_zG_c-2G_eG_y)y^2+\\
&+((8G_c\alpha^2G_e-4G_e(-G_c+G_a)\alpha-2G_bG_d)x^2+\\
&+((2G_yG_d-2G_eG_x)\alpha-2G_bG_z-16gG_c-2G_yG_d)x+\\
&+2gG_x+2G_z\alpha G_y-2G_zG_y)y-2x(-4\alpha G_d(1/2G_c-1/2G_a+G_c\alpha)x^2+\\
&+(-4G_z\alpha^2G_c+(G_dG_x+2G_z(-G_c+G_a))\alpha-gG_b)x+\\
&+G_xG_z\alpha-gG_y))z+G_e^2(-1+\alpha)^2y^4+2G_e(-1+)^2(G_z+G_dx)y^3+\\
&+(((G_e^2+G_d^2)\alpha^2-2\alpha G_d^2+G_d^2)x^2+(2G_dG_z+2G_d\alpha^2G_z-4G_dG_z\alpha-2gG_e)x+g^2+\\
&-2\alpha G_z^2+G_z^2\alpha^2+G_z^2)y^2+2x(G_z+G_dx)(\alpha^2G_ex-g)y+\\
&+x^2(G_d^2x^2\alpha^2+G_z^2\alpha^2+g^2+2G_z\alpha^2G_dx)].\end{aligned} \qquad \text{[A12]}$$

From Eq. [A12], some interesting cases can be analyzed separately

1. In the case typically encountered on clinical scanners, $g=0$, $\alpha=0.5$, and no quadratic SEMs are used. Therefore, $G_a=G_b=G_c=G_d=G_e=0$ and the concomitant field derived in (29) is obtained

$$B_c=\frac{1}{2B_0}\left(z^2(G_x^2+G_y^2)-zG_z(xG_x+yG_y)+G_z^2\frac{x^2+y^2}{4}\right). \quad [A13]$$

2. For a slice at the isocenter ($z=0$), B_c becomes

$$\begin{aligned}B_c=\frac{1}{2B_0}[&(-2G_e^2\alpha+G_e^2+G_e^2\alpha^2)y^4+((2\alpha^2G_dG_e-4G_dG_e\alpha+2G_eG_d)x+\\&-4G_eG_z\alpha+2G_eG_z+2\alpha^2G_zG_e)y^3+((\alpha^2G_d^2-2\alpha G_d^2+G_e^2\alpha^2+G_d^2)x^2+\\&+(-2G_eg+2G_dG_z+2G_dG_z\alpha^2-4\alpha G_dG_z)x-2\alpha G_z^2+\alpha^2G_z^2+G_z^2+g^2)y^2+\\&+(2x^3\alpha^2G_dG_e+(-2G_dg+2\alpha^2G_zG_e)x^2-2Gzxg)y+x^4\alpha^2G_d^2+2x^3\alpha^2G_zG_d+\\&+x^2(g^2+\alpha^2G_z^2)].\end{aligned} \quad [A14]$$

3. For a slice at the isocenter ($z=0$) and with $G_z=0$, B_c reduces to

$$\begin{aligned}B_c=\frac{1}{2B_0}[&(-2G_e^2\alpha+G_e^2+G_e^2\alpha^2)y^4+(2\alpha^2G_dG_e-4G_dG_e\alpha+2G_eG_d)xy^3+\\&+((\alpha^2G_d^2-2\alpha G_d^2+G_e^2\alpha^2+G_d^2)x^2-2xgG_e+g^2)y^2+\\&+(2x^3\alpha^2G_dG_e-2G_dgx^2)y+x^4\alpha^2G_d^2+x^2g^2].\end{aligned} \quad [A15]$$

4. When only quadratic SEMs are used for imaging ($G_x=0$, $G_y=0$, $G_z=0$), B_c is

$$\begin{aligned}B_c=\frac{1}{2B_0}[&(G_e^2-2G_e^2\alpha+\alpha^2G_e^2)y^4+((2G_eG_d+2\alpha^2G_dG_e-4G_dG_e\alpha)x+\\&+(12G_cG_e-20G_cG_e\alpha-4\alpha G_eG_a+8G_c\alpha^2G_e+4G_aG_e)z)y^3+\\&+((G_d^2+\alpha^2G_d^2-2\alpha G_d^2+\alpha^2G_e^2)x^2+((4G_aG_d+12G_dG_c-4\alpha G_dG_a+\\&-20G_cG_d\alpha-2G_bG_e+8G_c\alpha^2G_d)z-2gG_e)x+2gG_bz+\\&+(24G_aG_c+4G_a^2-2G_e^2+36G_c^2-48\alpha G_c^2+\\&+16\alpha^2G_c^2+G_b^2-16\alpha G_cG_a+2G_e^2\alpha)z^2+g^2)y^2+\\&+(((-4\alpha G_eG_a+8G_c\alpha^2G_e-2G_dG_b+4G_cG_e\alpha)z-2G_dg)x^2+\\&+((-16G_cG_b-2G_eG_d)z^2-16gG_cz)x+2x^3\alpha^2G_dG_e+\\&+(-12G_cG_e-4G_aG_e+2G_dG_b+8G_cG_e\alpha)z^3+2G_dgz^2)y+x^4\alpha^2G_d^2+\\&+(8G_c\alpha^2G_d-4\alpha G_dG_a+4G_cG_d\alpha)zx^3+(2gG_ez^2+\\&+(-4G_dG_c+2G_bG_e-8G_cG_d\alpha+4G_aG_d)z^3)x+(g^2+2gG_bz+\\&+(G_b^2-2\alpha G_d^2-16\alpha G_cG_a+4G_c^2+4G_a^2+16\alpha^2G_c^2+16\alpha G_c^2-8G_aG_c)z^2)x^2+\\&+(G_e^2+G_d^2)z^4].\end{aligned} \quad [A16]$$

5. When only the quadratic SEMs C2 and S2 are present ($G_x=0$, $G_y=0$, $G_z=0$, $G_c=0$, $G_d=0$, $G_e=0$), B_c is

$$B_c=\frac{1}{2B_0}(x^2+y^2)[z^2(4G_a^2+G_b^2)+2gG_bz+g^2]. \quad [A17]$$

6. If no z-dependent SEM is applied ($G_z=0$, $G_c=0$, $G_d=0$, $G_e=0$), B_c reduces to

$$B_c = \frac{1}{2B_0}[(4(G_a^2 + G_b^2)(x^2 + y^2) + 4(G_bG_y + G_aG_x)x + \\ +4(G_bG_x - G_aG_y)y + G_x^2 + G_y^2)z^2 + \\ +4g(x^2G_b + G_yx + y(G_x/2 + yG_b))z + g^2(x^2 + y^2)]. \quad [A18]$$

7. In the case the linear and the high-performance PatLoc SEM coil (19) are used for imaging ($G_d = 0$, $G_e = 0$) (33), B_c is

$$B_c(\vec{r}, t) = \frac{1}{2B_0}[((16\alpha^2G_c^2 + 24G_aG_c + G_b^2 + 4G_a^2 - 16\alpha G_cG_a + 36G_c^2 - 48\alpha G_c^2)z^2 + \\ +G_z^2 + g^2 + (4G_zG_a + 12G_zG_c - 4\alpha G_zG_a - 20\alpha G_zG_c + 8G_z\alpha^2G_c + 2gG_b)z + \\ -2\alpha G_z^2 + \alpha^2G_z^2)y^2 + (((-2G_bG_z - 16gG_c)z - 16G_cG_bz^2 - 2gG_z)x + \\ +(-12G_yG_c - 4G_aG_y + 8G_c\alpha G_y + 2G_bG_x)z^2 + \\ +(2G_z\alpha G_y + 2gG_x - 2G_zG_y)z)y + \\ +((2gG_b + 8G_z\alpha^2G_c - 4\alpha G_zG_a + 4\alpha G_zG_c)z + \\ +(G_b^2 + 4G_a^2 + 16\alpha G_c^2 - 8G_aG_c - 16\alpha G_cG_a + 16\alpha^2G_c^2 + 4G_c^2)z^2 + \\ +\alpha^2G_z^2 + g^2)x^2 + \\ +((-2\alpha G_zG_x + 2G_yg)z + (2G_bG_y + 4G_aG_x - 8\alpha G_cG_x - 4G_xG_c)z^2)x + \\ +(G_y^2 + G_x^2)z^2]. \quad [A19]$$

APPENDIX B

Concomitant Fields of the PatLoc SEM Coil

The partial derivatives of B_z with the three linear and the two quadratic encoding fields described by Eq. [7] for the PatLoc SEM coil (20) are

$$\frac{\partial B_z}{\partial x} = G_x + 4xG_\alpha\cos^2(\frac{\pi}{8}) - 4yG_\alpha\cos(\frac{\pi}{8})\sin(\frac{\pi}{8}) - 2xG_\alpha \\ +4yG_\beta\sin^2(\frac{\pi}{8}) + 4xG_\beta\cos(\frac{\pi}{8})\sin(\frac{\pi}{8}) - 2yG_\beta, \quad [B1]$$

$$\frac{\partial B_z}{\partial y} = G_y - 4xG_\alpha\cos(\frac{\pi}{8})\sin(\frac{\pi}{8}) - 4yG_\alpha\cos^2(\frac{\pi}{8}) + 2yG_\alpha \\ -4yG_\beta\cos(\frac{\pi}{8})\sin(\frac{\pi}{8}) + 4xG_\beta\cos^2(\frac{\pi}{8}) - 2xG_\beta, \quad [B2]$$

$$\frac{\partial B_z}{\partial z} = G_z. \quad [B3]$$

Note the difference of Eq. [A4] compared to Eq. [B3] because of the rotated SEM_α and SEM_β. The divergence equation of Maxwell's magnetostatics equations $\vec{\nabla} \cdot \vec{B} = 0$ requires

$$\frac{\partial B_x}{\partial x} + \frac{\partial B_y}{\partial y} + \frac{\partial B_z}{\partial z} = \frac{\partial B_x}{\partial x} + \frac{\partial B_y}{\partial y} + G_z = 0. \quad [B4]$$

By introducing the dimensionless parameter α in Eq. [B4], as in Eq. [A5], the same two constraints are introduced as with a linear SEM system (29)

$$\frac{\partial B_x}{\partial x} = -\alpha G_z \text{ and } \frac{\partial B_y}{\partial y} = G_z(\alpha - 1). \quad [B5]$$

The partial derivatives and the constraints from Maxwell's equations Eqs. [B4] and [2] gives the magnetic field vector length $||\vec{B}||$

$$||\vec{B}(\vec{r})|| = \sqrt{B_x^2 + B_y^2 + B_z^2} \\ = \sqrt{B_x^2 + B_y^2 + (B_0 + \sum_{i=x,y,z,\alpha,\beta}[\mathrm{SEM}_i \times G_i])^2} \\ = \sqrt{B_0^2(1+u)} \quad [B6]$$

$$\text{with} \quad u = \frac{B_x^2 + B_y^2}{B_0^2} + 2\frac{\sum_{i=x,y,z,\alpha,\beta}[\mathrm{SEM}_i \times G_i]}{B_0} + \\ \frac{(\sum_{i=x,y,z,\alpha,\beta}[\mathrm{SEM}_i \times G_i])^2}{B_0^2}. \quad [B7]$$

With the Taylor expansion of $\sqrt{1+u}$ given by Eq. [A9] and using Eq. [B7], the $||\vec{B}(\vec{r})||$ can be estimated similarly to Eq. [A10]. Using Eqs. [1] and [A11], the concomitant field B_c for the PatLoc SEM coil is

$$B_c = \frac{1}{2B_0}\Big(\Big[-x\alpha G_z + yg + z(G_x + G_\alpha\Big(\frac{\mu}{2}(\mu x - \nu y) \\ -\frac{\nu}{2}(\nu x + \mu y)\Big) + G_\beta\Big(\frac{\mu}{2}(\nu x + \mu y) + \frac{\nu}{2}(\mu x - \nu y)\Big)\Big)\Big]^2 \\ +\Big[xg - yG_z(1-\alpha) + z\Big(G_y - G_\alpha\Big(\frac{\nu}{2}(\mu x - \nu y) \\ +\frac{\mu}{2}(\nu x + \mu y)\Big) - G_\beta\Big(\frac{\nu}{2}(\nu x + \mu y) + \frac{\mu}{2}(\mu x - \nu y)\Big)\Big)\Big]^2\Big), \quad [B8]$$

with $\mu = \sqrt{2+\sqrt{2}}$ and $\nu = \sqrt{2-\sqrt{2}}$. One special case is the presence of only quadratic SEMs used for imaging ($G_x = 0$, $G_y = 0$, $G_z = 0$), which simplifies Eq. [B8] to

$$B_c(\vec{r}, t) = \frac{(x^2+y^2)[g^2 + z2\sqrt{2}g(G_\beta - G_\alpha) + z^2 4(G_\alpha^2 + G_\beta^2)]}{2B_0}. \quad [B9]$$

This is a slightly different result compared to Eq. [A17] which is the expression for the concomitant field calculated for second order spherical harmonics when $G_x = 0$, $G_y = 0$, $G_z = 0$, $G_c = 0$, $G_d = 0$, and $G_e = 0$. The difference lies only in the scaling coefficients of the spatial terms, which is a consequence of the physical rotation by $\pm\pi/8$ of the C2 and S2 SEMs of the PatLoc coil design (20).

REFERENCES

1. Mansfield P. Multiplanar image formation using NMR spin echoes. J Phys C: Solid State Phys 1977;10:L55–L58.
2. Ahn CB, Kim JH, Cho ZH. High-speed spiral-scan echo planar NMR imaging-I. IEEE Trans Med Imaging 1986;5:2–7.
3. Zahneisen B, Grotz T, Lee KJ, Ohlendorf S, Reisert M, Zaitsev M, Hennig J. Three-dimensional MR-encephalography: fast volumetric brain imaging using rosette trajectories. Magn Reson Med 2011;65: 1260–1268.
4. Zahneisen B, Hugger T, Lee KJ, LeVan P, Reisert M, Lee HL, Assländer J, Zaitsev M, Hennig J. Single shot concentric shells trajectories for ultra fast fMRI. Magn Reson Med 2012;68:484–494.
5. Assländer J, Zahneisen B, Hugger T, Reisert M, Lee HL, Levan P, Hennig J. Single shot whole brain imaging using spherical stack of spirals trajectories. Neuroimage 2013;73:59–70.
6. Duyn JH, Yang Y, Frank JA, van der Veen JW. Simple correction method for k-space trajectory deviations in MRI. J Magn Reson 1998; 132:150–153.
7. Norris DG, Hutchison JM. Concomitant magnetic field gradients and their effects on imaging at low magnetic field strengths. Magn Reson Med 1990;8:33–37.
8. Jezzard P, Barnett AS, Pierpaoli C. Characterization of and correction for eddy current artifacts in echo planar diffusion imaging. Magn Reson Med 1998;39:801–812.
9. King KF, Ganin A, Zhou XJ, Bernstein MA. Concomitant gradient field effects in spiral scans. Magn Reson Med 1999;41:103–112.
10. De Zanche N, Barmet C, Nordmeyer-Massner JA, Pruessmann KP. NMR probes for measuring magnetic fields and field dynamics in MR systems. Magn Reson Med 2008;60:176–186.
11. Sipilä P, Lange D, Lechner S, Löw W, Gross P, Baller M, Wachutka G, Wiesinger F. Robust, susceptibility-matched NMR probes for compensation of magnetic field imperfections in magnetic resonance imaging (MRI). Sens Actuators A Phys 2008;145–146:139–146.
12. Barmet C, De Zanche N, Pruessmann KP. Spatiotemporal magnetic field monitoring for MR. Magn Reson Med 2008;60:187–197.
13. Barmet C, De Zanche N, Wilm BJ, Pruessmann KP. A transmit/receive system for magnetic field monitoring of in vivo MRI. Magn Reson Med 2009;62:269–276.
14. Barmet C, Wilm BJ, Pavan M, Pruessmann KP. A third-order field camera with microsecond resolution for MR system diagnostics. In Proceedings of the 17th Annual Meeting of ISMRM, Honolulu, Hawai'i, USA, 2009. Abstract 781.
15. Han H, MacGregor RP, Balcom BJ. Pure phase encode magnetic field gradient monitor. J Magn Reson 2009;201:212–217.
16. Wilm BJ, Barmet C, Matteo P, Pruessmann KP. Higher order reconstruction for MRI in the presence of spatiotemporal field perturbations. Magn Reson Med 2011;65:1690–1701.
17. Testud F, Gallichan D, Barmet C, Vannesjö J, Welz AM, Cocosco CA, Pruessmann KP, Hennig J, Zaitsev M. Characterization of PatLoc gradient with a field camera. In Proceedings of the 20th Annual Meeting of ISMRM, Melbourne, Australia, 2012. Abstract 2598.
18. Hennig J, Welz AM, Schultz G, Korvink J, Liu Z, Speck O, Zaitsev M. Parallel imaging in non-bijective, curvilinear magnetic field gradients: a concept study. MAGMA 2008;21:5–14.
19. Zaitsev M, Punchard W, Dewdney A, Gallichan D, Stockmann JP, Cocosco CA, Littin S, Welz AM, Weber H, Starewicz P, Hennig J. Design and implementation of high-performance non-linear PatLoc gradient coil. In Proceedings of the 20th Annual Meeting of ISMRM, Melbourne, Australia, 2012. Abstract 2591.
20. Welz A, Cocosco C, Dewdney A et al. Development and characterization of An unshielded PatLoc gradient coil for human head imaging. Concepts Magn Reson Part B: Magn Reson Eng 2013;43:111–125.
21. Stockmann JP, Ciris PA, Galiana G, Tam L, Constable RT. O-space imaging: highly efficient parallel imaging using second-order nonlinear fields as encoding gradients with no phase encoding. Magn Reson Med 2010;64:447–456.
22. Stockmann JP, Galiana G, Tam L, Juchem C, Nixon TW, Constable RT. In vivo O-Space imaging with a dedicated 12 cm Z2 insert coil on a human 3T scanner using phase map calibration. Magn Reson Med 2013;69:444–445.
23. Schultz G, Ullmann P, Lehr H, Welz AM, Hennig J, Zaitsev M. Reconstruction of MRI data encoded with arbitrarily shaped, curvilinear, nonbijective magnetic fields. Magn Reson Med 2010;64:1390–1403.
24. Gallichan D, Cocosco CA, Dewdney A, Schultz G, Welz AM, Hennig J, Zaitsev M. Simultaneously driven linear and nonlinear spatial encoding fields in MRI. Magn Reson Med 2011;65:702–714.
25. Tam LK, Stockmann JP, Galiana G, Constable RT. Null space imaging: nonlinear magnetic encoding fields designed complementary to receiver coil sensitivities for improved acceleration in parallel imaging. Magn Reson Med 2012;68:1166–1175.
26. Lin FH. Multidimensionally encoded magnetic resonance imaging. Magn Reson Med 2013;70:86–96.
27. Layton KJ, Gallichan D, Testud F, Cocosco CA, Welz AM, Barmet C, Pruessmann KP, Hennig J, Zaitsev M. Single shot trajectory design for region-specifc imaging using linear and nonlinear magnetic encoding fields. Magn Reson Med 2013;70:684–696.
28. Gallichan D, Testud F, Barmet C, Cocosco CA, Welz AM, Pruessmann KP, Hennig J, Zaitsev M. Simultaneous linear and nonlinear encoding in a single shot. In Proceedings of the 20th Annual Meeting of ISMRM, Melbourne, Australia, 2012. Abstract 292.
29. Bernstein MA, Zhou XJ, Polzin JA, King KF, Ganin A, Pelc NJ, Glover GH. Concomitant gradient terms in phase contrast MR: analysis and correction. Magn Reson Med 1998;39:300–308.
30. Baron CA, Lebel RM, Wilman AH, Beaulieu C. The effect of concomitant gradient fields on diffusion tensor imaging. Magn Reson Med 2012;68:1190–1201.
31. Sica CT, Meyer CH. Concomitant gradient field effects in balanced steady-state free precession. Magn Reson Med 2007;57:721–730.
32. Meier C, Zwanger M, Feiweier T, Porter D. Concomitant field terms for asymmetric gradient coils: consequences for diffusion, flow, and echo-planar imaging. Magn Reson Med 2008;60:128–134.
33. Testud F, Gallichan D, Layton KJ, Welz AM, Barmet C, Cocosco CA, Pruessmann KP, Hennig J, Zaitsev M. Single shot multi-dimensional imaging using magnetic field monitoring and including Maxwell terms. In Proceedings of the 21th Annual Meeting of ISMRM, Salt Lake City, Utah, USA, 2013. Abstract 2598.
34. Hargreaves BA, Nishimura DG, Conolly SM. Time-optimal multidimensional gradient waveform design for rapid imaging. Magn Reson Med 2004;51:81–92.
35. Nistler J, Fontius U, Wald LL, Adalsteinsson E, Setsompop K, Alagappan VA, Hebrank F, Schmitt F, Renz W. Parallel transmission with an 8 channel whole body system at 3 T. In Proceedings of the Joint Annual Meeting of ISMRM-ESMRMB, Berlin, Germany, 2007. Abstract 1027.
36. Pruessmann KP, Weiger M, Börnert P, Boesiger P. Advances in sensitivity encoding with arbitrary k-space trajectories. Magn Reson Med 2001;46(4):638–651.
37. Walsh DO, Gmitro AF, Marcellin MW. Adaptive reconstruction of phased array MR imagery. Magn Reson Med 2000;43:682–690.
38. Weber H, Littin S, Galiana G, Feng J, Welz AM, Constable RT, Hennig J, Zaitsev M. 3D curved slice imaging. In Proceedings of the 21th Annual Meeting of ISMRM, Salt Lake City, Utah, USA, 2013. Abstract 2384.
39. Stone SS, Haldar JP, Tsao SC, Hwu WMW, Sutton BP, Liang ZP. Accelerating advanced MRI reconstructions on GPUs. J Parallel Distr Com 2008;68:1307–1318.
40. Bieri MA, Barmet C, Wilm BJ, Pruessmann KP. Versatile higher-order reconstruction accelerated by a graphics processing unit (GPU). In

Proceedings of the 19th Annual Meeting of ISMRM, Montréal, Canada, 2011. Abstract 2545.

41. Cocosco CA, Gallichan D, Testud F, Zaitsev M, Hennig J. GPUs open new avenues in medical MRI. In GPU Technology Conference (GTC), San Jose, California, USA, 2012. Abstract 348.
42. Cocosco CA, Dewdney A, Dietz P, Semmler P, Welz AM, Gallichan D, Weber H, Schultz G, Hennig J, Zaitsev M. Safety considerations for a PatLoc gradient insert coil for human head imaging. In Proceedings of the Joint Annual Meeting of ISMRM-ESMRMB, Stockholm, Sweden, 2010. Abstract 3946.
43. Cocosco CA, Gallichan D, Dewdney A, Schultz G, Welz AM, Witschey WR, Weber H, Hennig J, Zaitsev M. First in-vivo results with a PatLoc gradient insert coil for human head imaging. In Proceedings of the 19th Annual Meeting of ISMRM, Montréal, Canada, 2011. Abstract 714.
44. Gallichan D, Cocosco CA, Schultz G, Weber H, Welz AM, Hennig J, Zaitsev M. Practical considerations for in vivo MRI with higher dimensional spatial encoding. MAGMA 2012;25:419–431.
45. Welz AM, Testud F, Hennig J, Korvink J, Zaitsev M. Study of concomitant fields in multipolar PatLoc imaging. In Proceedings of the 20th Annual Meeting of ISMRM, Melbourne, Australia, 2012. p. 2597.
46. Barmet C, Wilm BJ, Pavan M, Pruessmann KP. Concurrent higher-order field monitoring for routine head MRI: an integrated heteronuclear setup. In Proceedings of the Joint Annual Meeting of ISMRM-ESMRMB, Stockholm, Sweden, 2010. Abstract 216.
47. Savitzky A, Golay MJE. Smoothing and differentiation of data by simplified least squares procedures. Anal Chem 1964;36:1627–1639.
48. Schneider JT, Haas M, Ruhm W, Hennig J, Ullmann P. Robust spatially selective excitation using radiofrequency pulses adapted to the effective spatially encoding magnetic fields. Magn Reson Med 2011; 65:409–421.
49. Sipilä P, Greding S, Wachutka G, Wiesinger F. 2H transmit-receive NMR probes for magnetic field monitoring in MRI. Magn Reson Med 2011;65:1498–1506.
50. Galiana G, Peters D, Tam LK, Constable RT. Multiecho acquisition of O-space data. Magn Reson Med 2014;72:1648–1657.